ABSTRACT

Title of Thesis: A MAGNETORHEOLOGICAL ENERGY ABSORBER FOR ENHANCED CRASHWORTHINESS IN DROP-INDUCED IMPACTS

Rebecca Marie Pierce
Master of Science, 2019

Thesis Directed By: Professor Norman M. Wereley
Department of Aerospace Engineering

This thesis uses a multidisciplinary approach to investigate the enhanced crashworthiness of a magnetorheological energy absorber (MREA). Magnetorheological (MR) fluids have been considered for use in crashworthiness applications because they can be modified to adjust for parameters such as an occupant's weight or the impact velocity of a crash. This study first reviews an existing soft landing control algorithm for an MREA vertically stroking crew seat and applies it to several crash scenarios. The combined addition of a bumper and optimized yield force is found to successfully reduce the jerk at the end of the MREA stroke without introducing new discontinuities in the acceleration profile. Secondly, this study explores the use of mesocarbon microbeads (MCMBs) in MR fluids. The MCMBs are found to increase the yield force produced in an MR damper. An endurance study further reveals the durability of the yield force-enhancing effect up to 100,000 cycles.

A MAGNETORHEOLOGICAL ENERGY ABSORBER FOR ENHANCED CRASHWORTHINESS IN DROP-INDUCED IMPACTS

by

Rebecca Marie Pierce

Thesis submitted to the Faculty of the Graduate School of the
University of Maryland, College Park in partial fulfillment
of the requirements for the degree of
Master of Science
2019

Advisory Committee:
Professor Norman M. Wereley, Chair/Advisor
Professor Alison B. Flatau
Professor Amr M. Baz

Acknowledgments

I would, first and foremost, like to thank my advisor, Dr. Norman Wereley for his advice and guidance through all of my projects during my graduate studies. I would also like to thank my thesis committee members, Dr. Baz and Dr. Flatau.

My first graduate school research project was with InnoVital Systems Inc. and I thank both Dr. Gregory Hiemenz and Pablo Sztein for enabling me to start my research and gain an appreciation for occupant protection and crashworthiness engineering. I would also like to acknowledge those who facilitated my research along the way: Dr. Ami Powell for teaching me how to use the rheometer and answering my questions, Dr. Young-Tai Choi for his guidance in working with MR fluids and dampers, and Mike Perna for his work in the machine shop, especially with modifying the MR dampers. Thanks also to Dr. Andrew Becnel who supported my interest in composites and additive manufacturing. I also express my gratitude toward Dr. Hsiao-Wen Chen who took me on as a research assistant before I started my graduate studies and supported me in my decision to apply to graduate school.

I would also like to acknowledge the UMD Vertical Lift Research Center of Excellence (VLRCOE), Army-Aviation Applied Technology Directorate, which partially supported this work under award number W911W61720004.

Thanks to all of my fellow graduate students who have made my time at the University of Maryland both enjoyable and intellectually interesting, particularly those who started the program with me and made my first year in graduate school better than I could have hoped for. I also owe the deepest gratitude to my lab

members for all of their support and friendship, whether it was through staying late at the laboratory or going to the gym together. I would particularly like to acknowledge Jon, Tom, Jacob, and Jacek.

Finally, I would like to thank my family and friends for their love and support over the years and their encouragement in pursuing a graduate education.

Table of Contents

List of Tables

List of Figures

List of Abbreviations

BP	Bingham Plastic
EA	Energy Absorber
CIP	Carbonyl Iron Particle
HB	Herschel-Bulkley
MCMB	Mesocarbon Microbead
MR	Magnetorheological
MREA	Magnetorheological Energy Absorber
MTS	Material Test System
SL	Soft Landing
YFO	Yield Force-Optimized

Chapter 1: Introduction

1.1 Helicopter Crashworthiness

Over the past sixty years, there has been a concerted effort to improve helicopter crashworthiness, beginning with the *Aircraft Crash Survival Design Guide* [1, 8] and continuing today with research on improved occupant protection systems [5, 9, 10]. Helicopter crashes can result in serious injury as high decelerative loads are transmitted through the floor and seat to an occupant's body. Crashworthiness advances in the area of occupant protection seek to mitigate the transmission of these loads. In general, a crashworthy helicopter design will implement a systems approach such as that shown in Figure 1.1 where the landing gear, subfloor, and seat work together to decelerate the occupant [2]. The seat is the final piece in the system and is responsible for limiting the decelerative loads experienced by the occupant [2]. Helicopter seats have thus been an integral part of crashworthiness research and include a variety of subparts such as occupant restraint systems [8], seat cushions [11], and seat suspensions [5]. This work will focus on seat suspensions encountering vertical loads.

Evaluating the effectiveness of a helicopter seat suspension is a multifaceted problem including the types of crashes the helicopter could undergo and the human

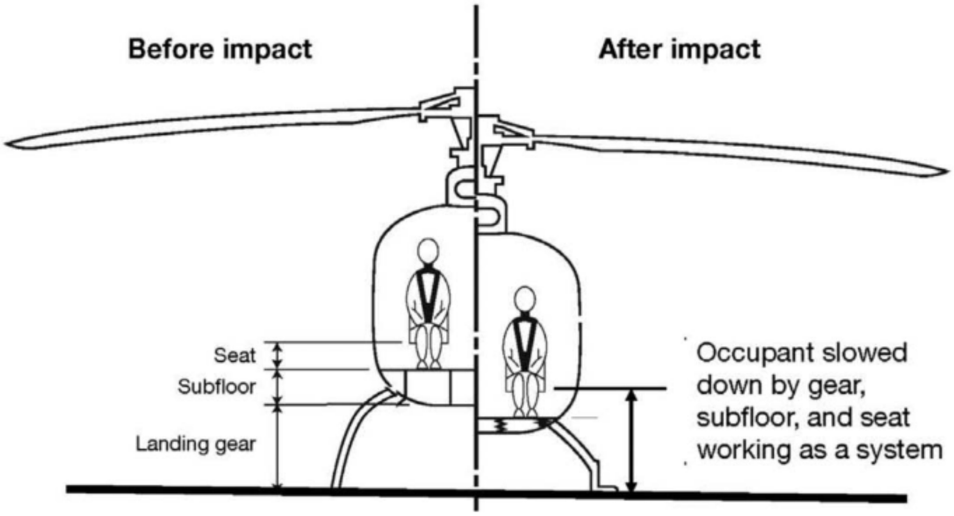

Figure 1.1: Systems approach to crashworthy design of a helicopter from [2]

tolerance to the shock conditions of those crashes. One factor used to characterize helicopter crash type is the initial drop velocity or sink rate (V_0), also known as the vertical velocity change (ΔV). The mean and 95th percentile survivable crash vertical velocity changes for four helicopters are shown in Table 1.1 which is adapted from [1] to include ΔV in m/s. At 8.8 and 14.4 m/s, the mean and 95th percentile ΔV experienced by the Sikorsky UH-60 Black Hawk are significantly higher than the mean and 95th percentile ΔV for the other three helicopters. According to military standard MIL-STD-1290, for rigid impacts with the landing gear extended, aircraft systems must have a vertical velocity change capability of 12.8 m/s (42 ft/s) without allowing more than a 15% reduction in occupant compartment height or exceeding accelerative load limits [12]. (Note that the 95th percentile ΔV for the UH-60 exceeds this design standard.) When the landing gear is not extended, the design standard reduces to 7.9 m/s (26 ft/s) [12].

Aircraft	Mean ΔV [m/s]	95th Percentile ΔV [m/s]
AH-1	4.1	12.0
OH-58	3.8	9.0
UH-1	3.5	10.2
UH-60	8.8	14.4

Table 1.1: Vertical velocity change in survivable crashes (adapted from [1])

While the initial drop velocity can serve to delineate crashes, it alone is not a sufficient predictor of the likelihood of injury. Human tolerance to impacts at any ΔV is often defined by the acceleration level. The relationship between acceleration level and injury, however, is complicated by the fact that injuries due to crashes can occur in any area of the body. One study by the U.S. Army Aeromedical Research Laboratory found that UH-60 and UH-1 cockpit crew involved in survivable ground impact mishaps experienced the highest percentage of serious or fatal injuries to the head and vertebral column [13]. The vertebral column, or spine, has been the focus of multiple injury criteria. The Dynamic Response Index (DRI) [14,15] and the 14.5 g deceleration limit load factor [16], two existing injury criteria which have been used to characterize vertical loads in aircraft, both evaluate the chance of spinal injury. The deceleration limit load provides one of the most straightforward assessments of injury likelihood in vertical impacts and will be employed in this work. While 23 g has been the accepted peak deceleration the human body can tolerate for more than 0.006 seconds, applying this limit to a seat suspension requires consideration of the seat's efficiency, η [16]. Desjardins and Harrison define efficiency as the average value divided by the peak value of the deceleration or load and find the seat to have an efficiency of 0.62 [16]. They further define the limit load factor using the average deceleration efficiency of the seat [16]. This results in a modified limit load of:

$$\bar{G} = \eta G_{peak} = (0.62)(23g) = 14.26\,g \approx 14.5\,g \tag{1.1}$$

Figure 1.2 [1,3] shows the correlation between this limit load factor and the rate of spinal injury with a 14.5 g load corresponding to a 20% injury rate for U.S. Army aviators.

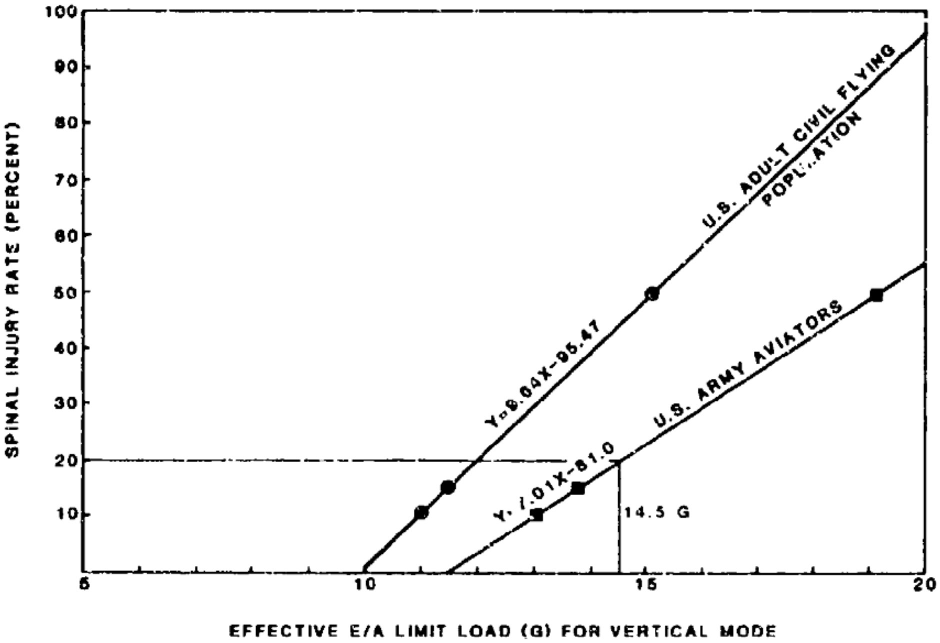

Figure 1.2: Correlation between the energy absorber limit load factor and spinal injury rate from [1,3]

While acceleration is the main injury-causing factor in helicopter crashes, studies have also investigated other factors such as the rate of change of acceleration (i.e. the jerk) [4,17]. The jerk is frequently considered in terms of the rate of onset of acceleration. In the 1950s, Eiband compiled data on human tolerance to rapidly applied accelerations in multiple directions (Figures 1.3-1.4) [4]. In the headward direction, lower rates of onset of acceleration have been found preferable to higher rates of onset (see Figure 1.3). In the tailward direction, rate of onset of acceleration has been closely correlated to peak accelerations with higher rates of onset combined with higher peak accelerations causing severe shock (see Figure 1.4). In experimental tests assessing the effect of jerk on the spine, Hodgson et al. find an experimental correlation between the dynamic load factor and jerk for lower levels of jerk, where the dynamic load factor is defined as the ratio of the peak to mean response and is examined both in terms of spinal acceleration and strain [17].

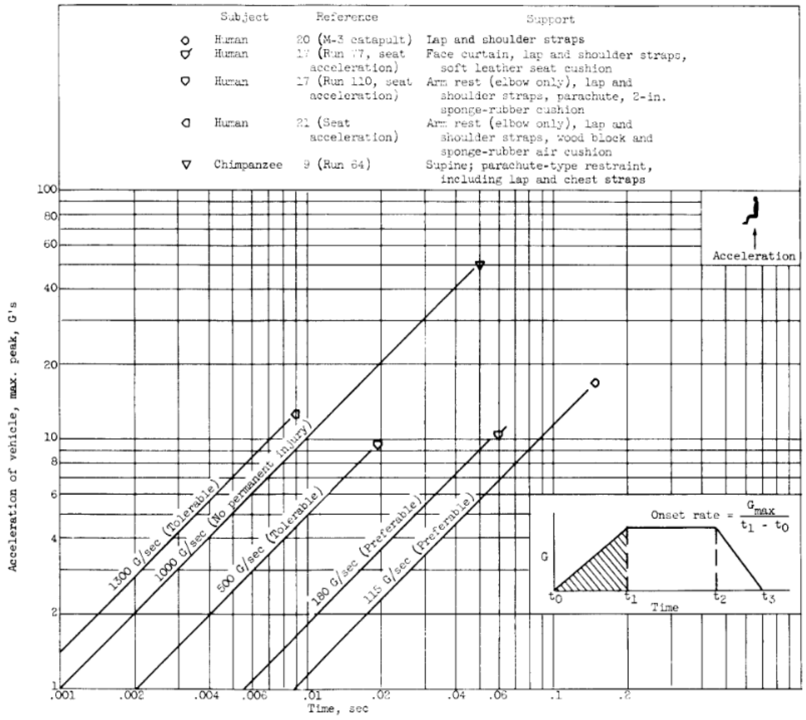

Figure 20. - Initial rate of change of headward acceleration endured by various subjects.

Figure 1.3: Effect of rate of onset of acceleration in the headward direction on injury from [4]

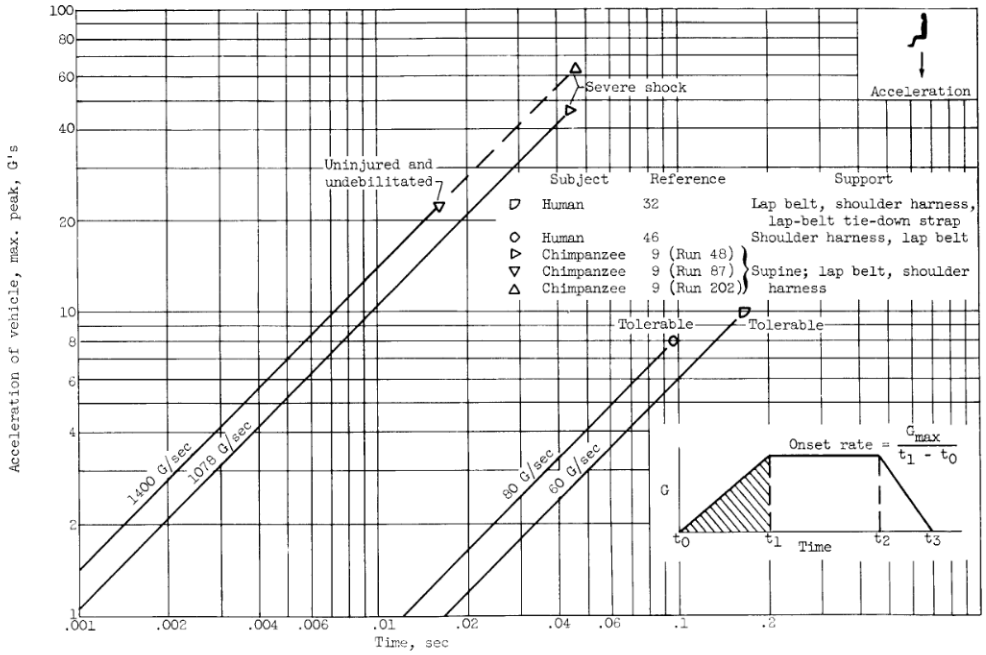

Figure 29. - Initial rate of change of tailward acceleration endured by various subjects.

Figure 1.4: Effect of rate of onset of acceleration in the tailward direction on injury from [4]

In an effort to increase occupant safety by reducing vertical load transmission to the occupant, energy attenuating (or energy absorbing) seats have been developed [18]. Examples of energy absorption devices for seat suspensions include wire-bending devices, inversion tubes, crushable honeycomb, housed pulleys, and composite tubes [8]. The U.S. Army incorporated energy attenuating seats as a requirement in the Utility Tactical Transport Aircraft System (UTTAS) program resulting in the UH60-A's crew seats [18]. Figure 1.5 depicts the energy-absorbing UH-60 crew seat designed by Simula, Inc. which employs inversion tubes [5]. Recently, magnetorheological devices have been investigated for use in aircraft seat suspensions [10, 19, 20]. While other energy absorbers have a fixed response, the force applied by a magnetorheological energy absorber can be varied based on occupant weight or crash type, facilitating a reduced probability of injury [20].

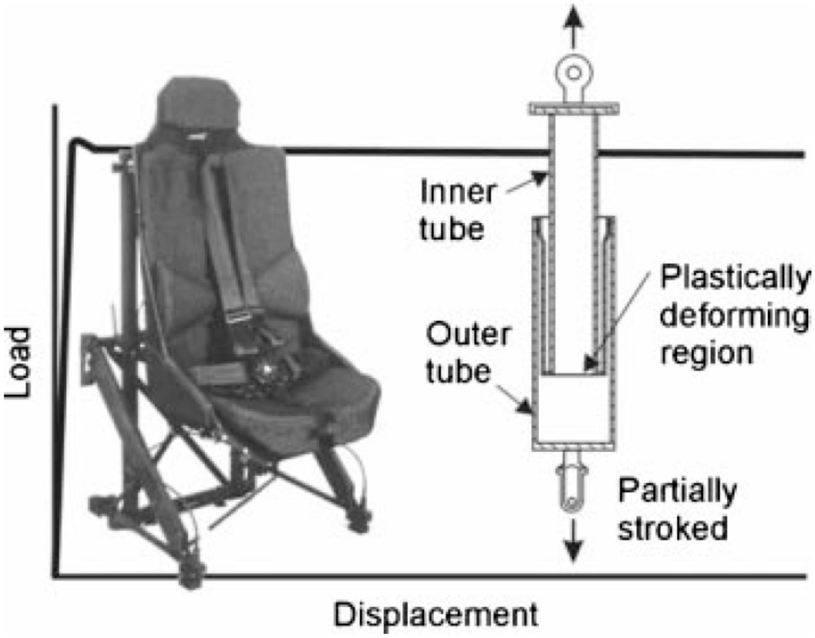

Figure 1.5: UH-60 crew seat with inversion tube and load-stroke profile from [5]

1.2 Magnetorheological Fluid

Magnetorheological (MR) fluids are fundamentally composed of magnetizeable particles, usually carbonyl iron, suspended in a carrier fluid. The carrier fluid is usually an oil such as silicon oil or a polyalfaolefin base oil. When a magnetic field is applied, the iron particles form chains aligned with the magnetic field lines (see Figure 1.6), thereby increasing the fluid's resistance to flow. MR fluids are thus desirable in variable damping applications such as MR seat suspensions [10,19], MR landing gear devices [21,22], and MR prosthetic devices [23].

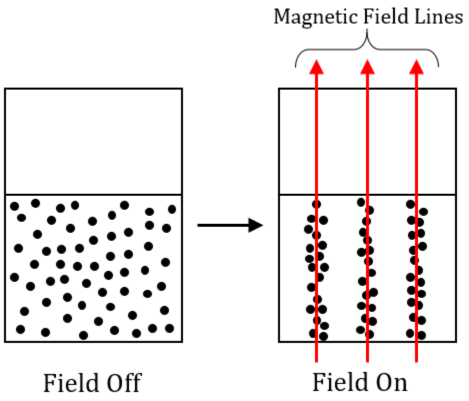

Figure 1.6: Field-based carbonyl iron particle alignment in an MR fluid

An MR fluid's resistance to flow can be characterized in two modes: shear mode (i.e. Couette flow, Figure 1.7(a)) and flow mode (i.e. Poiseuille flow, Figure 1.7(b)). Shear mode flow is tested in a rheometer, and flow mode can be tested in a device with a gap through which the fluid flows. Activated MR fluid can be characterized in shear mode by the yield stress, τ_y, which is the minimum stress required for the particle chains to break and the fluid to flow over parallel plates undergoing relative motion. Similarly, in flow mode, the yield force, f_y, is the minimum force required for the fluid to flow through a gap between two plates that are stationary relative to one another.

While their variable yield force allows MR fluids to be tailored for specific applications, this customization is limited by the fluid's durability, weight, working range, and sedimentation properties. Sedimentation has been well-researched with solutions such as using a bidisperse mixture of iron particle sizes [24] or adding surfactants such as fumed silica [25]. The range of the fluid is limited by magnetic

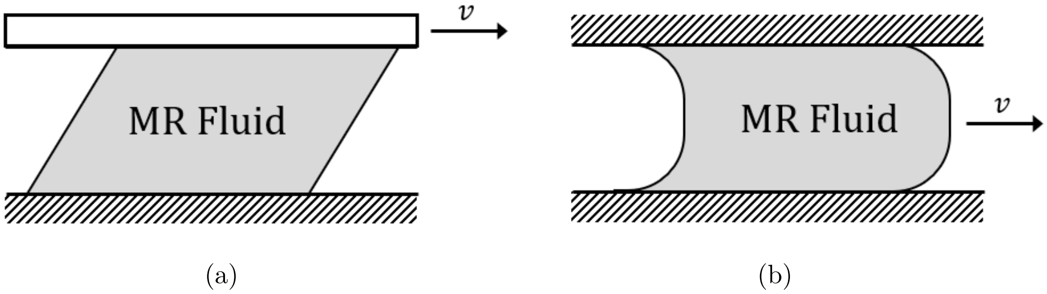

(a) (b)

Figure 1.7: MR fluid element in (a) shear mode (b) flow mode

saturation, at which point further increasing the current or magnetic field will no longer increase the yield force of the fluid [26]. Increasing the yield force is desirable because it enables the fluid to operate with a wider dynamic range at lower input current values.

A magnetorheological energy absorber for crashworthiness applications can take the form of a magnetorheological damper (see Figure 1.8). When the piston of an MR damper strokes in response to an applied field, the MR fluid flows through the gaps in the piston, represented by the flow mode fluid element shown in Figure 1.7(b). An increase in magnetic field strength will generally increase the force required for the particle chains to break and the piston to move through the fluid. MR dampers also often incorporate an accumulator at one end which is pressurized with nitrogen to prevent cavitation [27].

1.3 Magnetorheological Fluids and Helicopter Seat Suspensions

The implementation of magnetorheological technology in helicopter seat suspensions is an interdisciplinary challenge which can be divided into two main areas:

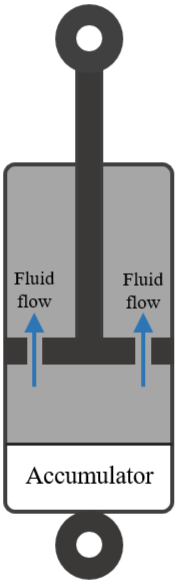

Figure 1.8: MR damper diagram

1. Development and testing of the MR fluid itself - The fluid must meet the design requirements for a particular aircraft. In general, research can include enhancement of the fluid to achieve higher yield force, reduced sedimentation, lower weight, and prolonged endurance.

2. Integration of an MR device onto the aircraft - This includes developments in mechanical design to developments in control algorithms. The control algorithms should be designed to the aforementioned injury criteria.

These two areas should work in tandem. The geometry of the helicopter and chosen control algorithm will influence the choice of MR fluid. Similarly, the properties of available MR fluids will influence what control algorithms are most applicable. This work incorporates elements from both of these areas, investigating the implementation and improvement of an existing MR device control algorithm and seeking to enhance the yield force and durability of an MR fluid while incurring less of a weight penalty.

1.4 Outline

The subsequent chapters of this thesis comprise a multifaceted investigation of a magnetorheological energy absorber for enhanced crashworthiness in drop-induced impacts and will be organized as follows:

- Chapter 2 - Overview of a Soft Landing Control Algorithm for a Magnetorheological Energy Absorber

  This chapter investigates an existing control algorithm for a magnetorheological energy absorber used in drop-induced impacts and details its uses and limitations.

- Chapter 3 - Modification of Soft Landing Control for Reduced Jerk

  This chapter builds upon the problem setup and control algorithm described in Chapter 2, adding a bumper and incorporating elements of engineering optimization to modify the yield force control for minimal jerk. A parametric study is also included to characterize the effects of varying the chosen bumper parameters.

- Chapter 4 - The Effect of Mesocarbon Microbeads on Magnetorheological Fluid

  This chapter investigates the yield force enhancement of MR fluid through the addition of passive particles. A study in the endurance characteristics of the fluid is also included.

- Chapter 5 - Conclusions

  This chapter offers conclusions and suggestions for future work.

Chapter 2: Overview of a Soft Landing Control Algorithm for a Magnetorheological Energy Absorber

2.1 Introduction

As described in Chapter 1, the development of energy absorbers (EAs) for use in helicopter seats has been an integral part of improving crashworthiness [18]. EAs can be passive, active, or semi-active. While passive EAs have a fixed load-stroke profile, semi-active EAs have tunable load-stroke profiles [20, 28]. Thus, instead of the impact response being predefined by the damping properties of the seat suspension, the damping properties of a semi-active suspension can be changed to match a desired impact response. One type of semi-active EA that has been explored over the past two decades is the magnetorheological energy absorber (MREA) [10,19,20]. In an MREA, the yield force is variable based on the applied magnetic field strength, enabling a helicopter seat suspension to be tailored based on individual occupant weights and crash impact velocities [20]. Browne et al. found a mixed mode MR damper to have a tunable stroking force at tested impact velocities of 1-10 m/s [28]. Designing an MREA-based helicopter seat suspension involves the development of a suitable control algorithm to meet the desired seat response objectives.

Existing methods of controlling magnetorheological devices in helicopter seat suspensions are skyhook control [10], a constant stroking load regulator (CSLR) [29], and initial Bingham number, or yield force, control [19, 20]. The latter two control algorithms were developed with the objective of attaining a 'soft landing', defined as reaching zero velocity at the maximum stroke of the damper [19, 20]. The CSLR [29] varies the yield force while maintaining a constant acceleration and initial Bingham number control keeps the yield force constant while decreasing the acceleration [19, 20]. Both algorithms control the yield force or its nondimensional counterpart, the Bingham number.

The 'soft landing' objective reduces an occupant's potential for injury in a twofold manner: coming to a stop by the end of the stroke avoids an end-stop impact and using the full stroke facilitates lower peak decelerative loads [19, 20]. While this capability has been successfully demonstrated by Wereley, Choi, and Singh [19, 20], no restrictions have been made on the acceleration or jerk. More specifically, there is no limit on the peak acceleration or on the acceleration at the end of the stroke. This chapter presents the initial Bingham number 'soft landing' (SL) control method, hereafter referred to as SL control, and its limitations for a given available stroke length and damping constant of the MREA. The results of SL control are examined with respect to occupant weight and injury criteria.

2.2 Problem Definition: Initial Drop Velocity Magnetorheological Energy Absorber with 'Soft Landing' Control

This section applies the initial Bingham number 'soft landing' control method developed in [19,20] to an MREA vertically stroking crew seat impacting the ground at initial drop velocities ranging from 4-13 m/s (13.1-42.7 ft/s). As outlined in the introduction, 12.8 m/s (42 ft/s) is the military design requirement based on the 95th percentile of crash velocities [12]. Figure 2.1 depicts this MREA configuration with an initial drop velocity of V_0 in the negative x direction. The force due to the MREA, F_{MREA}, is composed of a passive damping component and a yield force component. The passive damping constant of the MREA, c_{MR}, is 900 Ns/m and the yield force, f_y, is determined using the control algorithm. The payload mass, m, is 77 kg, based on the mass of a 50th percentile male. The maximum stroke length, S, is 40.64 cm (16 in), based on the available stroke length of the UH-60

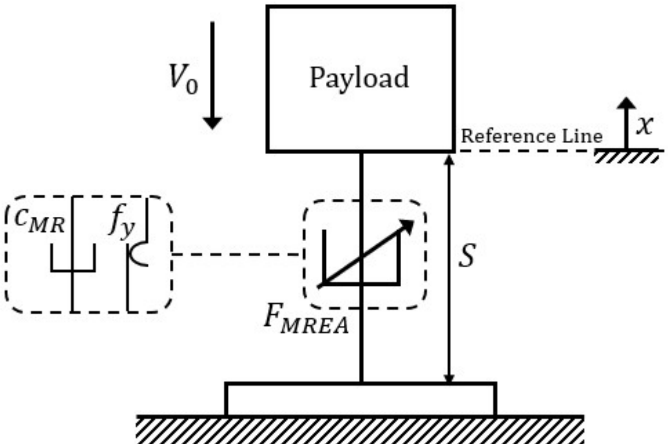

Figure 2.1: MREA vertically stroking crew seat

Black Hawk [18].

The governing equation for this setup is

$$m\ddot{x} + c_{_{MR}}\dot{x} + f_y \operatorname{sgn}(\dot{x}) + mg = 0 \tag{2.1}$$

where $\operatorname{sgn}(\dot{x})$ is the signum function defined as

$$\operatorname{sgn}(\dot{x}) = \begin{cases} -1 & \dot{x} < 1 \\ 0 & \dot{x} = 0 \\ 1 & \dot{x} > 0 \end{cases} \tag{2.2}$$

If $\dot{x} = V$, Equation 2.1 can be re-written as

$$\dot{V} + \frac{c_{_{MR}}}{m} V = -\frac{\big(mg + f_y \operatorname{sgn}(V)\big)}{m} \tag{2.3}$$

Integrating Equation 2.3 and using the initial condition $V(0) = -V_0$ (see Appendix A for the full derivation) leads to

$$V = -V_0 e^{-tc_{_{MR}}/m} - \frac{\big(mg + f_y \operatorname{sgn}(V)\big)}{c_{_{MR}}}\Big(1 - e^{-tc_{_{MR}}/m}\Big) \tag{2.4}$$

Integrating again and using the initial condition $x(0) = 0$ (see Appendix A for the full derivation) leads to

$$x = -\frac{V_0 m}{c_{_{MR}}}(1 - e^{-tc_{_{MR}}/m}) - \frac{(mg + f_y \operatorname{sgn}(V))}{c_{_{MR}}}\Big(t - \frac{m}{c_{_{MR}}} + \frac{m}{c_{_{MR}}} e^{-tc_{_{MR}}/m}\Big) \tag{2.5}$$

Implementing the ‘soft landing’ condition that the velocity must be zero at the end of the seat response $V(t_f) = 0$ and solving Equation 2.4 for t_f (see Appendix A for the full derivation), yields

$$t_f = \frac{m}{c_{_{MR}}} \ln\left(1 - \frac{c_{_{MR}} V_0}{mg + f_{y,opt} \operatorname{sgn}(V)}\right) \tag{2.6}$$

where $f_{y,opt}$ is the optimal yield force defined as the applied yield force which will result in a ‘soft landing’. Using the second ‘soft landing’ condition, that the

MREA must fully utilize the stroke, Equation 2.5 can be solved for the yield force:

$$\begin{aligned} f_{y,opt}\,\mathrm{sgn}(V) = &-\frac{V_0 m}{t_f}(1-e^{-t_f c_{MR}/m}) \\ &-\frac{(mg+f_{y,opt}\,\mathrm{sgn}(V))m}{t_f c_{MR}}(-1+e^{-t_f c_{MR}/m}) - mg + \frac{S c_{MR}}{t_f} \end{aligned} \tag{2.7}$$

SL control manipulates the seat response such that the stroke is always downwards, meaning that the velocity is always negative and $\mathrm{sgn}(V) = -1$. Equations 2.4-2.7 can then be simplified to

$$V = -V_0 e^{-t c_{MR}/m} + \frac{f_y - mg}{c_{MR}}(1-e^{-t c_{MR}/m}) \tag{2.8a}$$

$$x = -\frac{V_0 m}{c_{MR}}(1-e^{-t c_{MR}/m}) + \frac{f_y - mg}{c_{MR}}\left(t - \frac{m}{c_{MR}} + \frac{m}{c_{MR}}e^{-t c_{MR}/m}\right) \tag{2.8b}$$

$$t_f = \frac{m}{c_{MR}}\ln\left(1 - \frac{V_0 c_{MR}}{mg - f_{y,opt}}\right) \tag{2.8c}$$

$$f_{y,opt} = \frac{V_0 m}{t_f}(1-e^{-t_f c_{MR}/m}) + \frac{(mg - f_{y,opt})}{t_f}\frac{m}{c_{MR}}(e^{-t_f c_{MR}/m} - 1) + mg - \frac{S c_{MR}}{t_f} \tag{2.8d}$$

The expression for $f_{y,opt}$ must be solved for iteratively. $f_{y,opt}$ is often reported in non-dimensional form as the Bingham number, defined in [20] as

$$Bi = \frac{f_y}{c_{MR} V_0} \tag{2.9}$$

One concern in seat suspension design is the possibility of an end-stop impact. SL control is intended to eliminate this possibility. Wereley et al. model an end-stop impact as an underdamped mass-spring-damper system which describes the payload's displacement, velocity, and acceleration at the maximum stroke, after the end-stop impact has occurred [20]. These values are functions of the payload displacement and velocity at the full stroke, before the end-stop impact has occurred and result in the following values if the 'soft landing' conditions are met:

$$\begin{aligned} x^{+} &= x^{-} \\ v^{+} &= v^{-} = 0 \\ a^{+} &= 0 \end{aligned} \tag{2.10}$$

where the superscript $(-)$ indicates maximum stroke before the end-stop impact and the superscript $(+)$ indicates maximum stroke after the end-stop impact. Because the $(-)$ and $(+)$ values occur at the same displacement, they should be equivalent if the function is continuous. While the displacement and velocity at this point are continuous by definition for SL control, the acceleration is only continuous if $a^{-} = 0$. If $a^{-} \neq 0$, the acceleration will be discontinuous and result in an uncontrolled jerk. The principal function of the end-stop impact model when SL control is used is to bring the acceleration down to zero. It does not influence the displacement or velocity.

Using Equations 2.8a-2.8d and the 'soft landing' end-stop model in Equation 2.10, the optimum yield force and payload response are determined for initial drop velocities of 4-13 m/s. Figure 2.2 shows the resulting displacement, velocity, acceleration, and jerk resulting from SL control of the MREA vertically stroking crew seat with a 50th percentile male occupant undergoing an initial drop velocity of 9 m/s. The displacement and velocity curves validate that SL control produces the desired 'soft landing' where the damper reaches zero velocity at maximum displacement. With a 9 m/s initial drop velocity, the acceleration profile falls beneath the 14.5 g limit load. It is notable, however, that the acceleration at the end of the stroke is nonzero. If the end-stop model from Wereley et al. is used to bring the acceleration to zero, an uncontrolled level of jerk would result. This phenomenon is represented

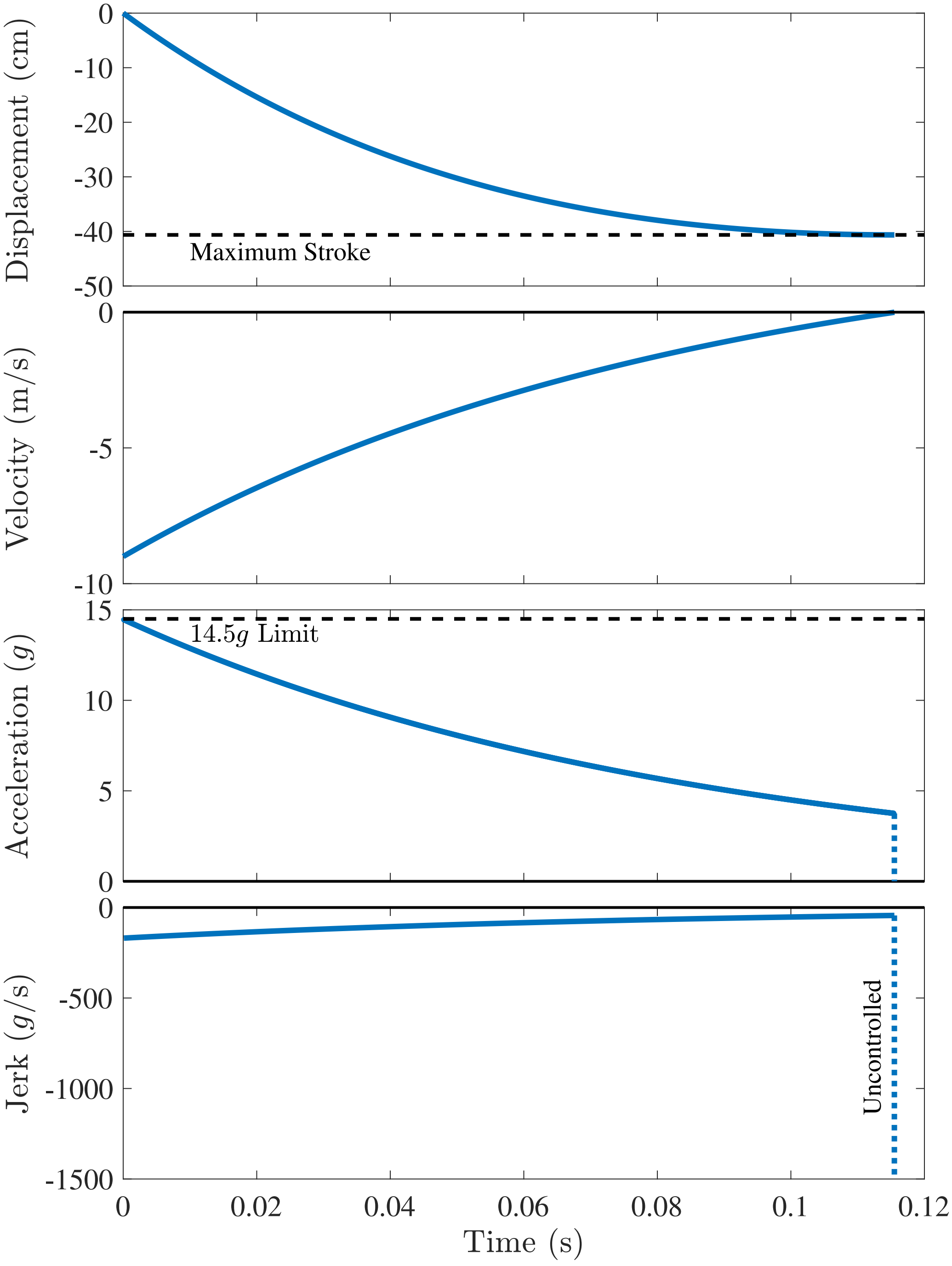

Figure 2.2: Results of SL control for a 50th male occupant with $V_0 = 9$ m/s and $c_{MR} = 900$ Ns/m

in Figure 2.2 by the dashed lines in the acceleration and jerk plots. In Figure 2.2, the uncontrolled level of jerk is plotted up to -1500 g/s, but the calculation is an artifact of the time step chosen for evaluation. The jerk could thus be much higher, particularly if the drop in acceleration is considered to be instantaneous.

2.3 Effectiveness of SL Control Over a Variety of Occupant Weights

To determine the effectiveness of the given setup and control algorithm for occupants other than the 50th male, the optimal yield forces required to achieve a 'soft landing' across initial drop velocities of 4-13 m/s are determined for a 5th percentile female and 95th percentile male occupant with weights of 47 and 97 kg, respectively. Figure 2.3(a) shows the peak accelerations required to reach the 'soft landing' conditions as a function of initial drop velocity for the three occupant weights. There are no solutions for the 5th female at a V_0 range of 4-7 m/s or for the 50th male at a V_0 of 4 m/s because the MREA passive damping constant of 900 Ns/m is to high to satisfy the 'soft landing' conditions; a velocity of zero is reached before the full stroke is used (see Equations 2.6 and 2.7). Figure 2.3(b) also reveals that at and above 8 m/s, the peak acceleration experienced by the 5th female exceeds the 14.5 g limit load. Above 9 m/s, the acceleration levels experienced by the 50th male and 95th male also exceed 14.5 g. Table 2.1 lists the V_0 ranges for which a solution exists with a peak acceleration below the 14.5 g limit load. Within the given problem parameters, SL control yields no solutions within the injury criteria for the 5th female. The 50th male and 95th male have solutions within the 14.5

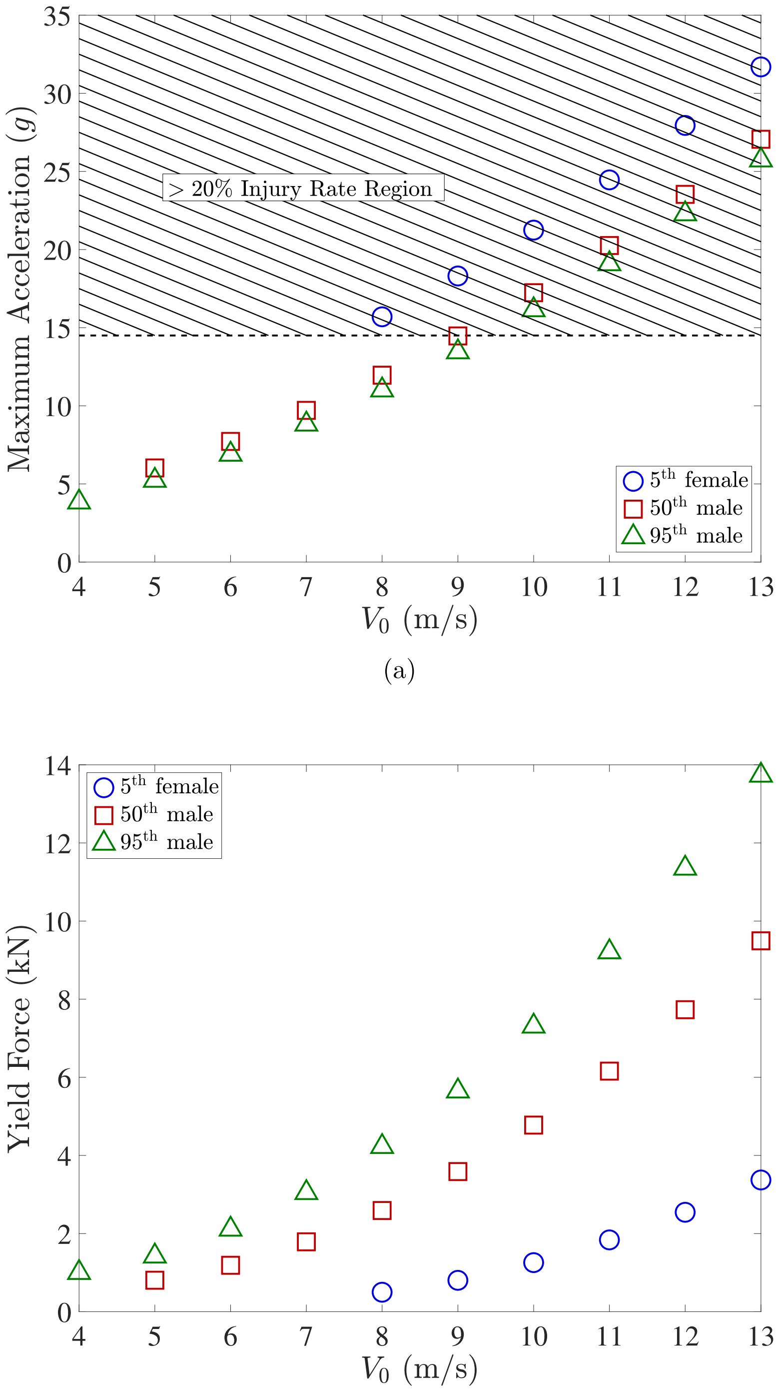

(a)

(b)

Figure 2.3: (a) Peak accelerations and (b) optimal yield forces resulting from SL control with $c_{_{MR}} = 900$ Ns/m

g limit load for V_0 ranges of 5-9 m/s and 4-9 m/s, respectively. It is clear that the usefulness of SL control is limited by the passive damping of the MREA being controlled. The V_0 ranges of functionality can be widened if the passive damping of the MREA is lowered from the current 900 Ns/m to 500 Ns/m as shown in Figure 2.4(a). However, Figure 2.4(b) reveals that decreasing the passive damping constant of the MREA would increase the optimal yield forces required to reach a 'soft landing'. This introduces the challenge of creating an MREA which has low passive damping but capabilities for very high yield forces. Lowering the passive damping of the MREA also increases the end level acceleration as seen in Figure 2.5 which plots the results for the 50th male at 9 m/s when $C_{MR} = 500$ Ns/m.

Occupant	Range of V_0 with a Feasible Solution with Peak Accelerations Below 14.5 g
5th female	——
50th male	5-9 m/s
95th male	4-9 m/s

Table 2.1: Range of Acceptable Solutions for Each Occupant

It is also evident in both Figure 2.3(b) and Figure 2.4(b) that the optimal yield forces increase as occupant weight increases. A much wider range of yield forces is required for the 95th male to achieve a 'soft landing' than for the 5th female to achieve the same.

2.4 The Benefits and Limitations of SL Control

The preceding investigation of SL control for an MREA with a stroke length of 40.64 cm and a passive damping constant of 900 Ns/m exhibits the algorithm's

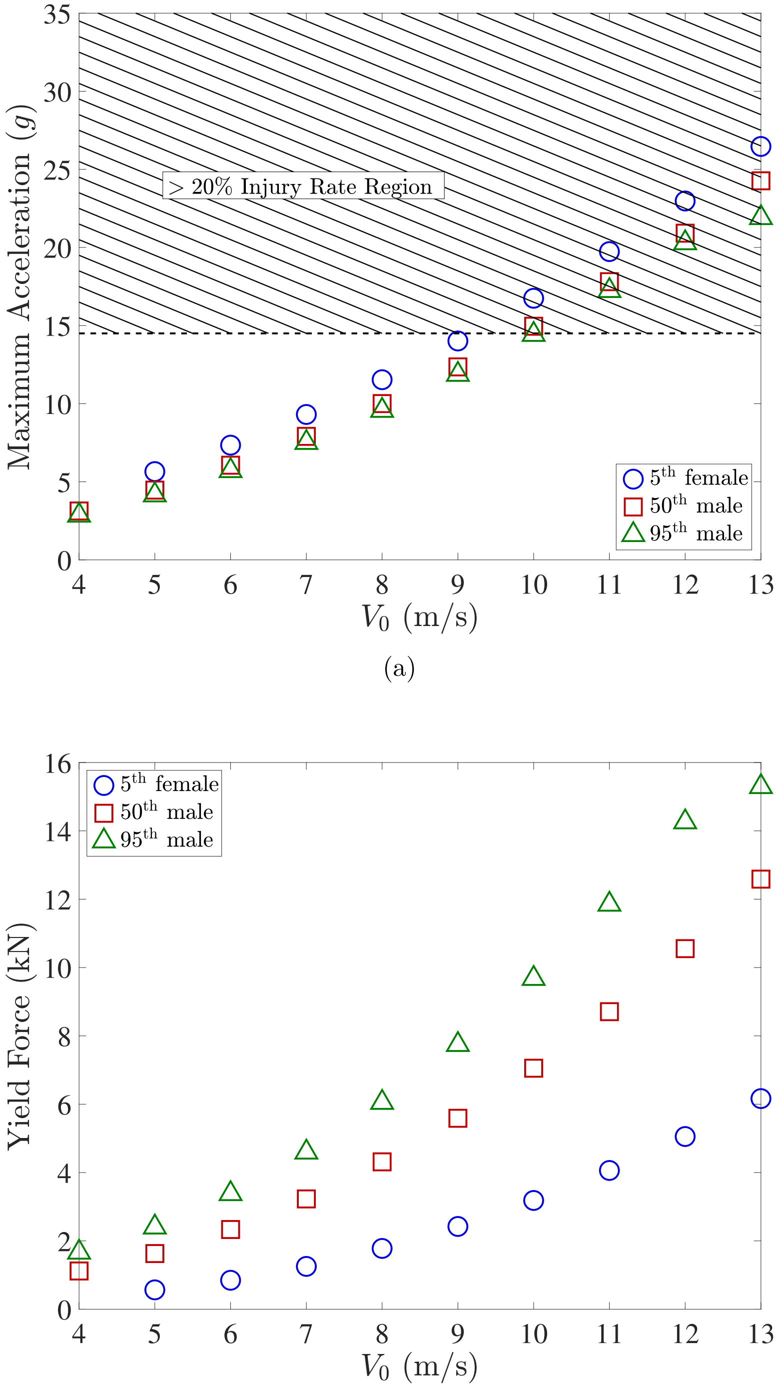

(a)

(b)

Figure 2.4: (a) Peak accelerations and (b) optimal yield forces resulting from SL control with $c_{MR} = 500$ Ns/m

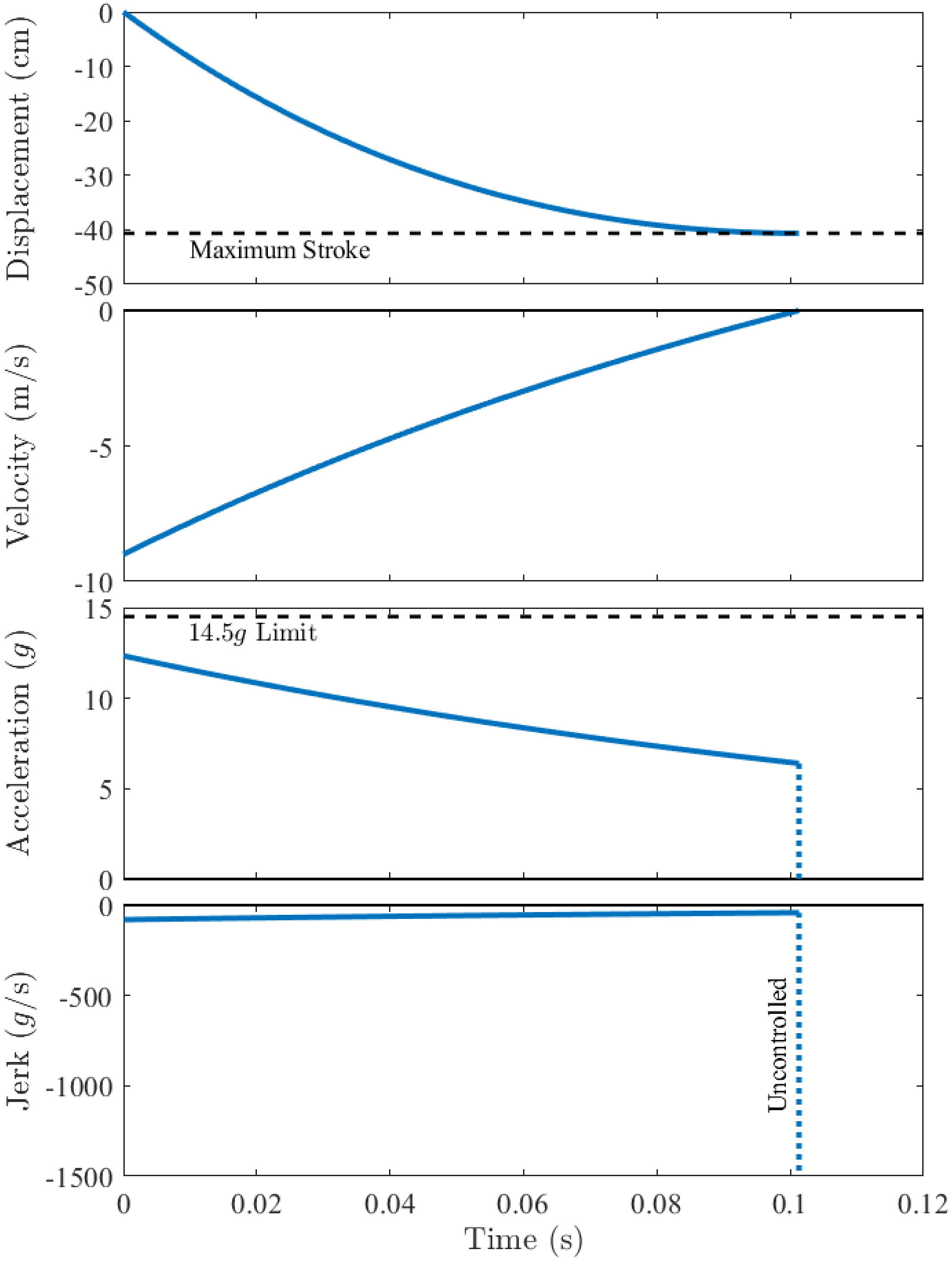

Figure 2.5: SL control for a 50th male occupant with $V_0 = 9$ m/s and $c_{MR} = 500$ Ns/m

capability to bring an occupant to a stop at the full stroke of the device in a simple and mathematically elegant manner. There are however several limitations to the implementation of SL control. The combination of drop velocities and occupant weights for which a solution is feasible is dependant on the passive damping of the MREA. While SL control does theoretically reduce accelerations by distributing the load over the full stroke, it also does not directly account for injury criteria. Furthermore, SL control does not constrain the acceleration profile, meaning that the acceleration at the 'soft landing' point can be several gs. If an end-stop model is incorporated which brings the acceleration to zero, there is an uncontrolled level of jerk. SL control is thus limited in its functionality, though valid in its restrictions on displacement and velocity. Chapter 3 details potential modifications of SL control to reduce the jerk and presents an analysis of the range of V_0 for which a feasible solution is obtained.

Chapter 3: Modification of Soft Landing Control for Reduced Jerk

3.1 Introduction

Chapter 2 illustrated how SL control determines the yield force necessary for an MREA vertically stroking crew seat to bring the velocity of the payload down to zero while using the full available stroke. However, it is limited in its application range and can result in a high end level acceleration, producing an uncontrolled level of jerk. It has been suggested that jerk can affect occupant comfort [30] and, in the case of vehicle suspensions, noise [31]. In the domain of semi-active suspensions, such as MREAs, several algorithms have been suggested for reducing the jerk between the off- and on-states of the skyhook control algorithm [31–33]. This reduction of jerk has focused on vibration isolators, and no methods exist for mitigating the jerk at the end of the seat response in SL control. This chapter investigates the addition of a bumper and modification of the optimal yield force to minimize the peak jerk levels while adhering to the 'soft landing' criteria as closely as possible.

These objectives form a constrained minimization problem which is suitable for the application of optimization techniques. Multiple research studies have explored the intersection of engineering optimization and magnetorheological technology. Such research has ranged from optimizing the damper geometry [34, 35] to optimizing the control algorithm for the MR device [36, 37]. In one previous application of optimization techniques to MR seat suspension control, Singh et al. optimized the variation of yield force with displacement to obtain maximum safety for a 95th percentile male occupant experiencing a shock due to a 5 m/s drop velocity and found the optimal control of the yield force to be a linear function of seat stroke [36]. Optimization techniques have also been used to determine the optimality of multiple existing semi-active vehicle suspension control algorithms [38]. It is evident that MR seat suspension control algorithms can benefit from optimization. The current work takes a similar approach to that of Singh et al. [36], investigating the optimization of yield force to produce minimal jerk within given constraints.

This chapter's investigation into the minimization of jerk will be divided as follows. Section 3.2 details the setup and results of adding a bumper towards the end of the MREA stroke while maintaining the same initial drop velocity-dependent optimal yield forces determined in Chapter 2. Section 3.3 sets up the yield force optimization problem for minimizing peak jerk and presents the results. The response is also examined with respect to an established injury criteria. In Section 3.4, a parametric study is included to evaluate the sensitivity of the solution to the properties of the bumper. Section 3.5 examines the effectiveness of the optimization scheme across multiple occupant weights.

3.2 Vertically Stroking MREA with Bumper

This section explores the addition of a bumper during the last 2.54 cm (1 in) of MREA stroke as a method of reducing the acceleration and jerk at the end of the stroke. During this final portion of the stroke, the magnetic field is turned off so that $f_y \operatorname{sgn}(\dot{x}) = 0$ and the MREA only contributes a force due to the passive damping ($c_{_{MR}}\dot{x}$). The distance to the bumper from the reference line, b, is 38.10 cm (15 in). The model of the MREA vertically stroking crew seat with end bumper is shown in Figure 3.1.

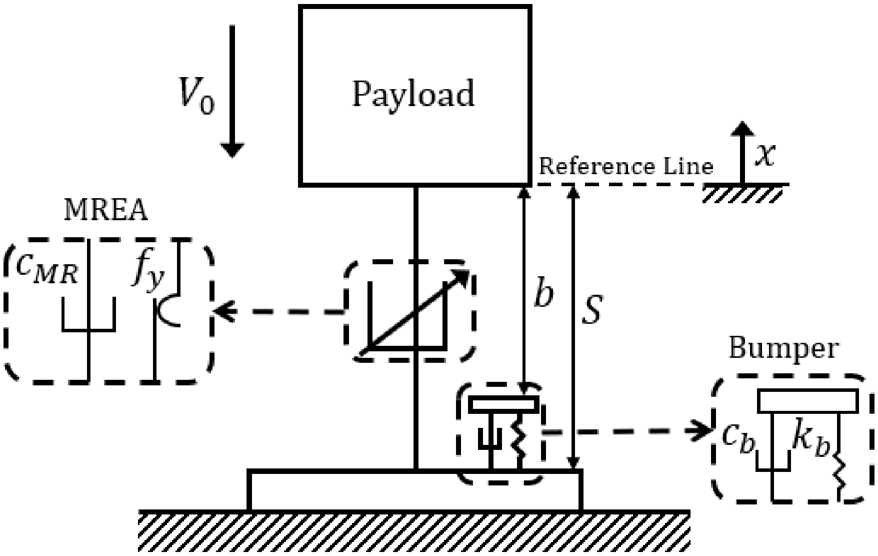

Figure 3.1: MREA with bumper setup

To describe the motion of the mass when in contact with the bumper, a new coordinate, x_b, is defined which is zero at the uncompressed position of the bumper. The transformation between x and x_b is $x_b = x - b$. Figure 3.2 shows the payload when in contact with the bumper.

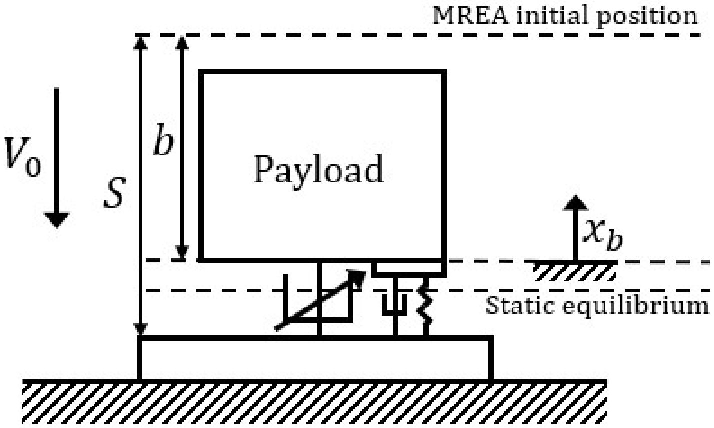

Figure 3.2: MREA with bumper and modified coordinate system

The response during this period is governed by the following equation:

$$m\ddot{x}_b + (c_{_{MR}} + c_b)\dot{x}_b + k_b x_b + mg = 0 \tag{3.1}$$

The governing equation can be re-formulated to represent the fact that the bumper does not start at its equilibrium position [39]:

$$m\ddot{x}_b + (c_{_{MR}} + c_b)\dot{x}_b + k_b\left(x_b + \frac{mg}{k_b}\right) = 0; \tag{3.2}$$

To obtain the homogeneous solution, this equation can be re-written using the variable transformation $y = x_b + \frac{mg}{k_b}$. The governing equation then becomes

$$m\ddot{y} + (c_{_{MR}} + c_b)\dot{y} + k_b y = 0 \tag{3.3}$$

If the system is underdamped, the solution takes the following form outlined in [39]:

$$\begin{gathered} y(t) = Ce^{-\zeta\omega_n t}\cos(\omega_d t - \phi) \\ \text{where } C = \sqrt{(y_0)^2 + \left(\frac{\zeta\omega_n y_0 + \dot{y}_0}{\omega_d}\right)^2} \text{ and } \phi = \tan^{-1}\left(\frac{\zeta\omega_n}{\omega_d} + \frac{\dot{y}_0}{\omega_d y_0}\right) \end{gathered} \tag{3.4}$$

where y_0 is the initial displacement and $\dot{y}_0$ is the initial velocity defined as the displacement and velocity values when the MREA reaches its maximum stroke, before impacting the bumper. ζ is the damping ratio of the system, ω_n is the natural frequency defined as $\sqrt{k_b/m}$, and $\omega_d = \omega_n\sqrt{1-\zeta^2}$. In the absence of the MREA, the damping ratio of the bumper would be

$$\zeta_b = \frac{c_b}{2\sqrt{mk_b}} \tag{3.5}$$

However, because the MREA does contribute to the passive damping, a new total damping ratio can be defined as

$$\zeta = \frac{c_{MR} + c_b}{2\sqrt{mk_b}} \tag{3.6}$$

Integrating Equation 3.4 yields the velocity and acceleration solutions:

$$\begin{aligned} \dot{y}(t) &= -Ce^{-\zeta\omega_n t}\Big[\zeta\omega_n \cos(\omega_d t - \phi) + \omega_d \sin(\omega_d t - \phi)\Big] \\ \ddot{y}(t) &= Ce^{-\zeta\omega_n t}\Big\{\Big[(\zeta\omega_n)^2 - \omega_d^2\Big]\cos(\omega_d t - \phi) + \Big[2\zeta\omega_n\omega_d\Big]\sin(\omega_d t - \phi)\Big\} \end{aligned} \tag{3.7}$$

So, the overall setup of the MREA with a bumper is modeled using the following piecewise function:

$$\ddot{x} = \begin{cases} -\frac{c_{MR}}{m}\dot{x} - \frac{f_y}{m}\operatorname{sgn}(\dot{x}) - g & x^- \geq -b \\ -\frac{(c_{MR}+c_b)}{m}\dot{x} - k_b(x - b + \frac{mg}{k_b}) & x^+ \leq -b \end{cases} \tag{3.8}$$

Figure 3.3 shows the resulting response of a 50th percentile male to a 9 m/s impact if the optimal yield force calculated in SL control is used until contact with the bumper (at which point it is switched off) and a bumper with a stiffness of $k_b = 150$ kN/m and damping ratio of $\zeta_b = 0.3$ (total damping ratio of $\zeta = 0.432$)

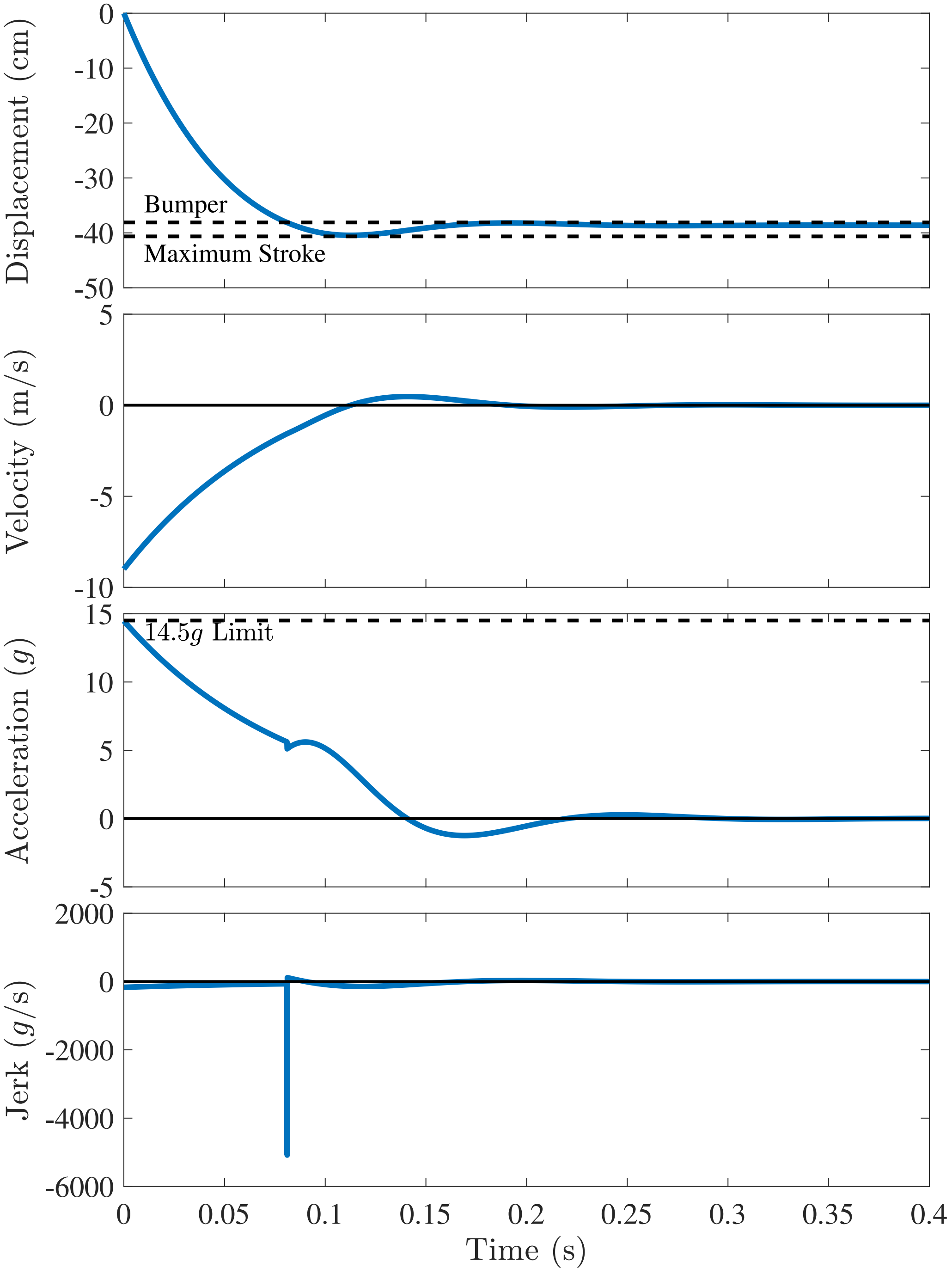

Figure 3.3: SL Control with added bumper for a 50th male with $V_0 = 9$ m/s

is added to the system. The displacement, velocity, acceleration, and jerk follow the SL control-defined curves until the MREA makes contact with the bumper.

The addition of the bumper successfully brings the end acceleration down to zero, mitigating the end level jerk. However, while the acceleration and jerk at the end of the stroke are brought down to zero, a new spike in the jerk is introduced from the discontinuity in acceleration when the MREA contacts the bumper.

3.3 Optimization to Reduce Jerk

In order to reduce the newly introduced jerk at the transition from the MREA-dominated to the bumper-dominated regions, an optimization problem is formulated to determine a new optimal yield force, $f_{y,opt}$, that minimizes the peak magnitude of the jerk. In standard form, this optimization problem is written as:

$$\begin{aligned} \text{minimize} \quad & \max(|\dddot{x}|) \\ \text{subject to:} \quad & \\ & g_1 : |\dot{x}(t_f)| - 0.001 \leq 0 \\ & g_2 : x(t_f) + b \leq 0 \\ & g_3 : -\min(x) - S \leq 0 \\ & g_4 : \max(x(t_b : t_f)) + b \leq 0 \\ & g_5 : |\ddot{x}(t_b) - \ddot{x}(t_b + \Delta t)| - 0.2 \leq 0 \end{aligned} \tag{3.9}$$

where t_b is the time the bumper is contacted, t_f is the final time simulated, and Δt is the time step (defined in this problem as 0.0001 seconds). g_i form the set of inequality constraints for this problem. The first two inequality constraints are modified 'soft landing' conditions. g_1 requires the final velocity to be zero with a tolerance of 1 mm/s. g_2 constrains the MREA to, at minimum, utilize all of the available stroke up to the bumper position. The third inequality constraint restricts the maximum stroke utilization to the available stroke length. The fourth constraint restricts the rebound of the bumper to a maximum at the bumper's initial resting location. The final inequality constraint, g_5, requires the acceleration to be relatively continuous at the transition to the bumper-dominated portion of the stroke. Additional bound constraints are added limiting the optimal yield force to the range of 0.0001 N $\leq x \leq$ 25000 N.

The problem is formulated as a penalty transformation optimization problem which minimizes the objective function while simultaneously penalizing constraint violations [40]. A typical penalty function will follow the form outlined in [40]:

$$T(\mathbf{x}, r) \triangleq f(\mathbf{x}) + r^{-1}P(\mathbf{x}), \qquad r > 0 \tag{3.10}$$

where $f(\mathbf{x})$ is the objective function, r is a weighting parameter, $P(\mathbf{x})$ is the penalty function, and $\mathbf{x}$ is the vector of design variables. $P(\mathbf{x})$ will often take the form of a quadratic loss function for inequality constraints and a similar form for equality constraints [40]:

$$P(\mathbf{x}) \triangleq \begin{cases} \sum_{j=1}^{m} [\max\left(0, g_j(\mathbf{x})\right)]^2 & \forall\ g_j(\mathbf{x}) \\ \sum_{k=1}^{n} [h_k(\mathbf{x})]^2 & \forall\ h_k(\mathbf{x}) \end{cases} \tag{3.11}$$

These constraints are weighted more heavily as r decreases. If all the inequality and equality constraints are satisfied, the penalty function will be zero and will have no effect on $T(\mathbf{x}, r)$ irrespective of the value of r. The minimum of Equation 3.10 can be found by choosing a monotonically decreasing sequence for r and following the subsequent steps:

1. Provide initial values of $\mathbf{x}$ and r.

2. Minimize $T(\mathbf{x}, r)$. (This work uses MATLAB's `fminsearch` unconstrained

optimizer [41].)

3. Test for convergence. If the function has converged, a minimum satisfying the constraints has been found. If the function has not converged, use the solution as the new initial guess and use the next value of r in the sequence to increase the penalization of the constraints.

A solution which satisfies all constraints will converge because $P(\mathbf{x})$ will be zero. If the solution diverges, the minimum found by the optimizer likely violates one or more constraints. The penalty formulation for the minimization of jerk can thus be written as

$$minimize \quad \max(|\dddot{x}|) + r^{-1}\left(\sum_{j=1}^{4}\left(\max(0, g_j)\right)^2\right) \tag{3.12}$$

All inequality constraints are normalized by their limiting values [42]. For example, the inequality constraint $x \leq a$ can be written as

$$\frac{x}{a} \leq 1 \tag{3.13}$$

In standard form, this becomes

$$\frac{x}{a} - 1 \leq 0 \tag{3.14}$$

Similarly, $x \geq b$ can be written in standard form as:

$$1 - \frac{x}{b} \leq 0 \tag{3.15}$$

Solving this optimization problem for a 50th male occupant and a crash with a 9 m/s initial drop velocity results in Figure 3.4. The magnitude of the peak jerk has reduced significantly from the SL control case, while reducing any disconstinuties in acceleration introduced by the bumper. The velocity and displacement profiles before the MREA contacts the bumper do not change significantly from those produced using SL control. Figures 3.5-3.6 show the results of this yield force-optimized (YFO) control for the 50th male and impact velocities of 4-13 m/s. Table 3.1 gives the convergence information for the optimization scheme. Above 9 m/s, the constraints, particularly the the maximum stroke utilization (g_3) and maximum bumper rebound (g_4), begin to be violated. The violation of g_3 results in an infeasible solution because an end-stop impact would occur, causing an undesirable spike in the levels of acceleration and jerk.

One limitation of the optimization routine is the possibility of finding a local minimum because the optimizer can be sensitive to the initial guess for yield force. The optimization routine may also find a local minimum when convergence is not reached and the constraints are not satisfied. For example, the 10 m/s solution given by YFO control for the 50th male did not follow the trend for peak jerk. This yield force was thus adjusted until the peak jerk fell within the trend evident in Figure 3.5(a). The maximum stroke utilization and peak acceleration plots were adjusted accordingly.

It is evident that the YFO control of an MREA vertically stroking crew seat with a bumper can successfully bring the acceleration and jerk down to zero at the end of the stroke.

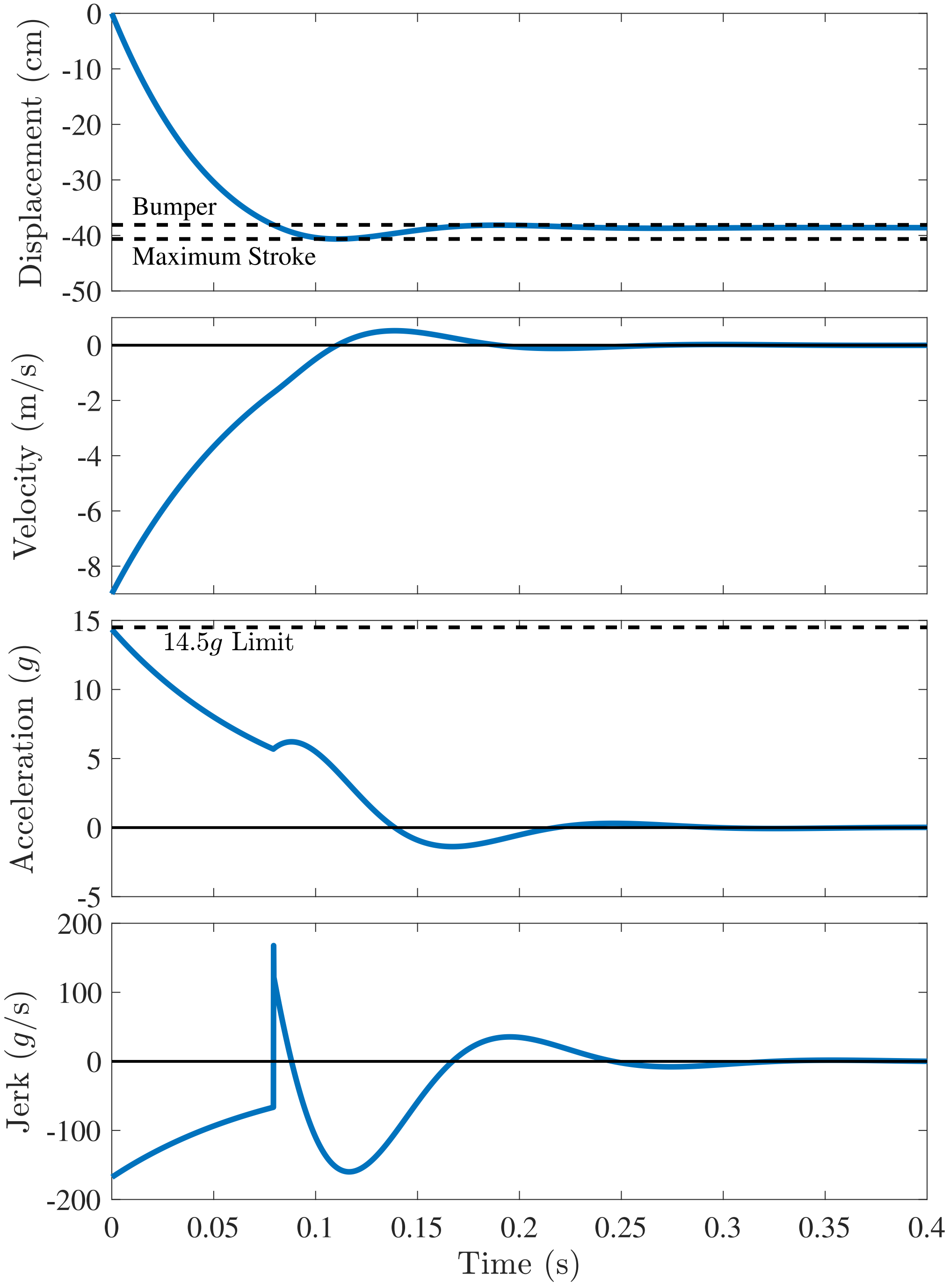

Figure 3.4: Results of YFO control of MREA with added bumper for a 50th male with $V_0 = 9$ m/s

ΔV [m/s]	Convergence	Constraints Violated
4	Yes	—
5	Yes	—
6	Yes	—
7	Yes	—
8	Yes	—
9	Yes	g_3 active (tolerance=10^{-4}))
10	Yes	g_3, g_4
11	Yes	g_3, g_4, g_5
12	No	g_3, g_4
13	No	g_3, g_4

Table 3.1: Convergence details of YFO control for a 50th male

3.4 Parametric Study

A parametric study is included to characterize the effect of k_b and ζ on the seat response and to explore the possibility of extending the capabilities of the MREA under YFO control, thereby increasing the range of drop velocities for which realistic solutions are available. The stiffness of the bumper is varied from 50 kN/m to 1000 kN/m and the damping constant is varied from 0.1-0.6. Material feasibility is not included in this study, but would need to be considered in further work, with the available materials bounding the possible stiffness and damping values. The affected values that are considered are: the peak acceleration, peak magnitude of jerk, maximum displacement, and optimal yield force.

1. Stiffness

   Figures 3.7 and 3.8 show the results of changing the bumper stiffness. Increasing the stiffness of the bumper results in higher maximum magnitude of the jerk, increased peak acceleration levels, decreased maximum stroke uti-

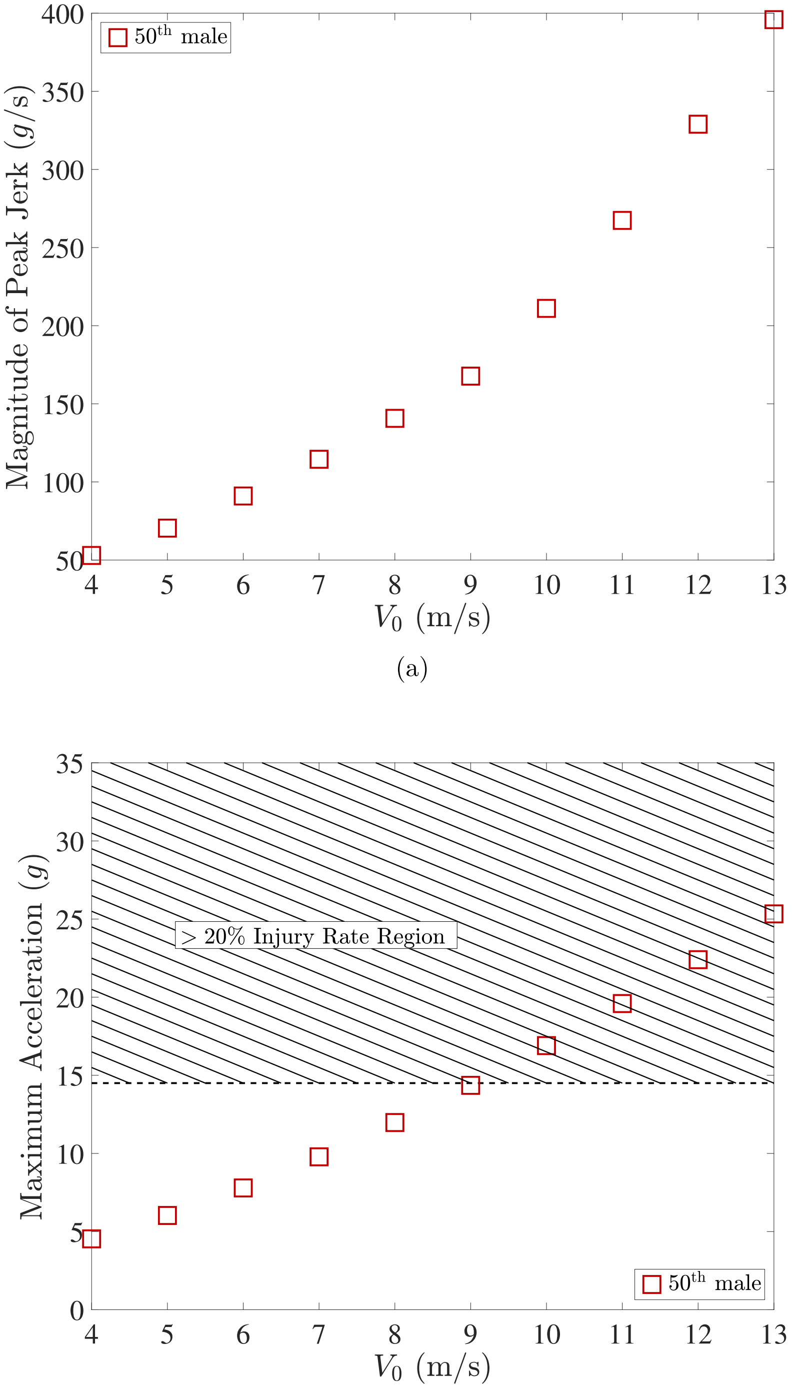

(a)

(b)

Figure 3.5: YFO Control jerk and peak acceleration results for a 50th male

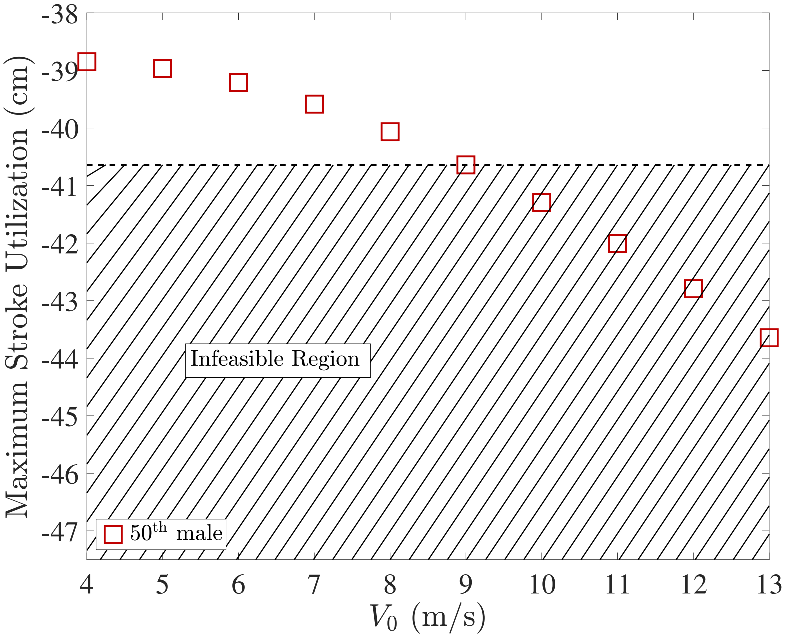

(a)

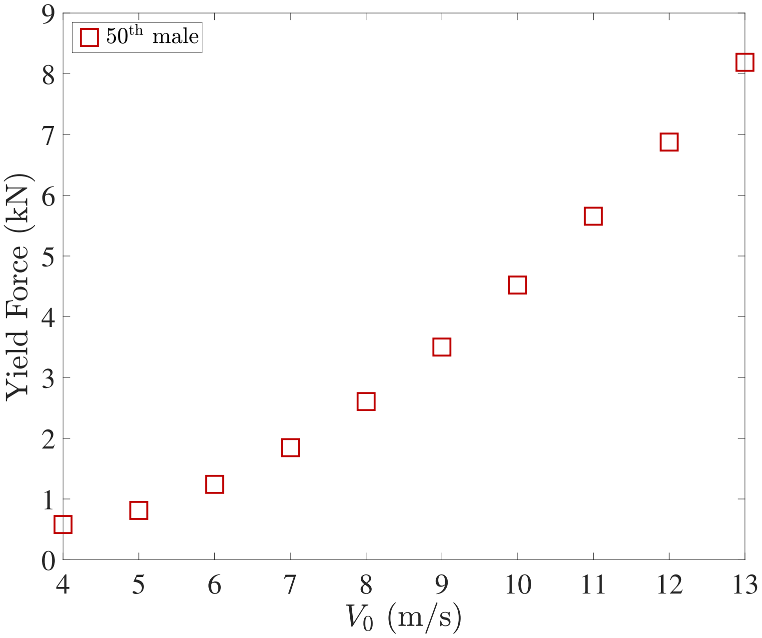

(b)

Figure 3.6: YFO Control stroke utilization and optimal yield force results for a 50th male

lization, and increased optimal yield force values. The values of V_0 for which the penalty method minimization converged are included in Table 3.2

k_b [kN/m]	V_0s with converged solutions [m/s]
50	4-5
100	4-7
150	4-9
200	4-10
500	4-9
1000	4-11

Table 3.2: Convergence details when varying k_b

2. Damping Ratio

   Increasing the damping ratio of the bumper, ζ_b increases the peak acceleration, decreases the stroke utilization, and increases the yield force. There is not a clear overall trend in the relationship between jerk and ζ_b, although the lowest damping ratio generally results in the highest jerk levels.

ζ_b [ ]	V_0s with converged solutions [m/s]
0.1	4-5
0.2	4-7
0.3	4-9
0.4	4-10
0.5	4-11
0.6	4-13

Table 3.3: Convergence details when varying ζ_b

The overall trends discovered in the parametric studies are included in Table 3.4. Both parametric studies show a trade-off in feasibility: a higher damping ratio or yield force will result in more solutions which do not violate the maximum stroke

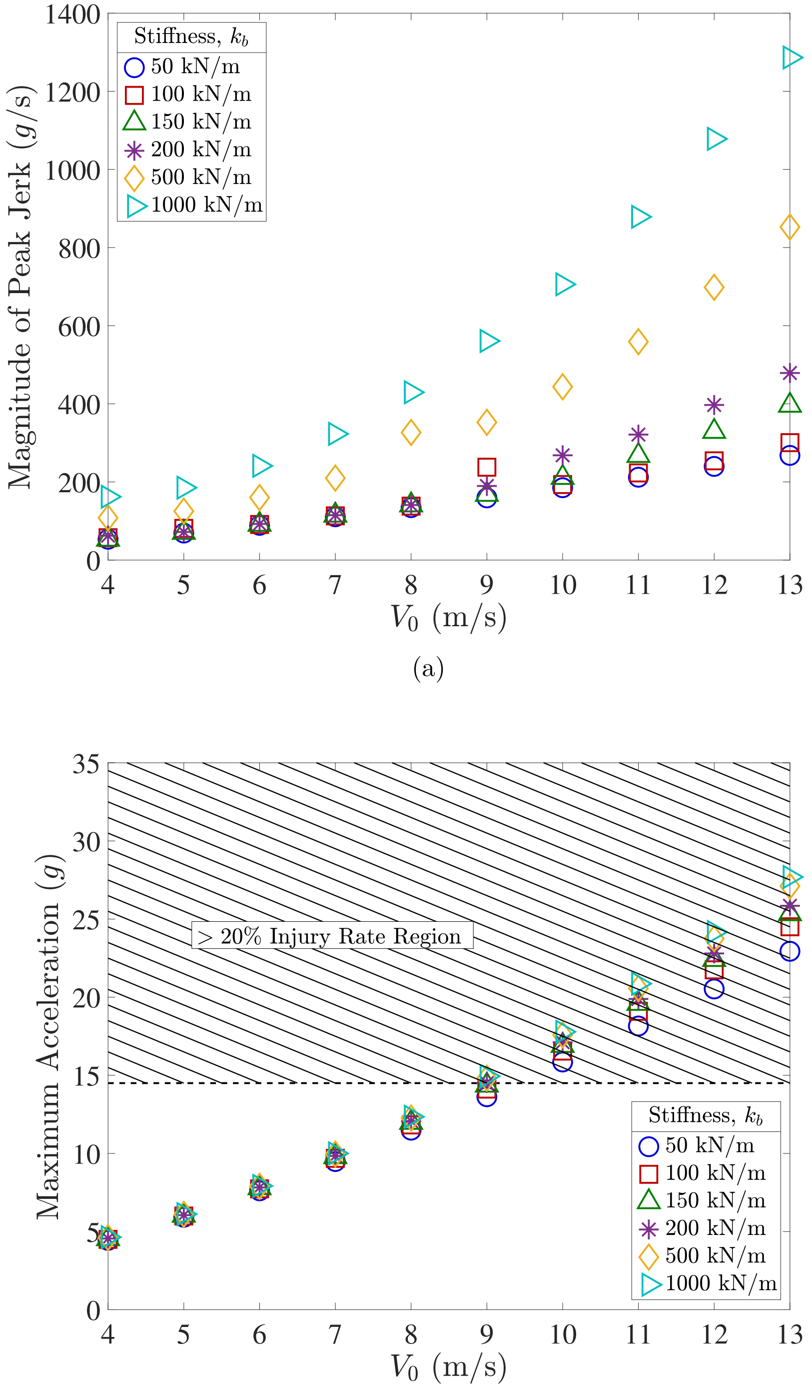

(a)

(b)

Figure 3.7: Jerk and peak acceleration results from parametric study of k_b

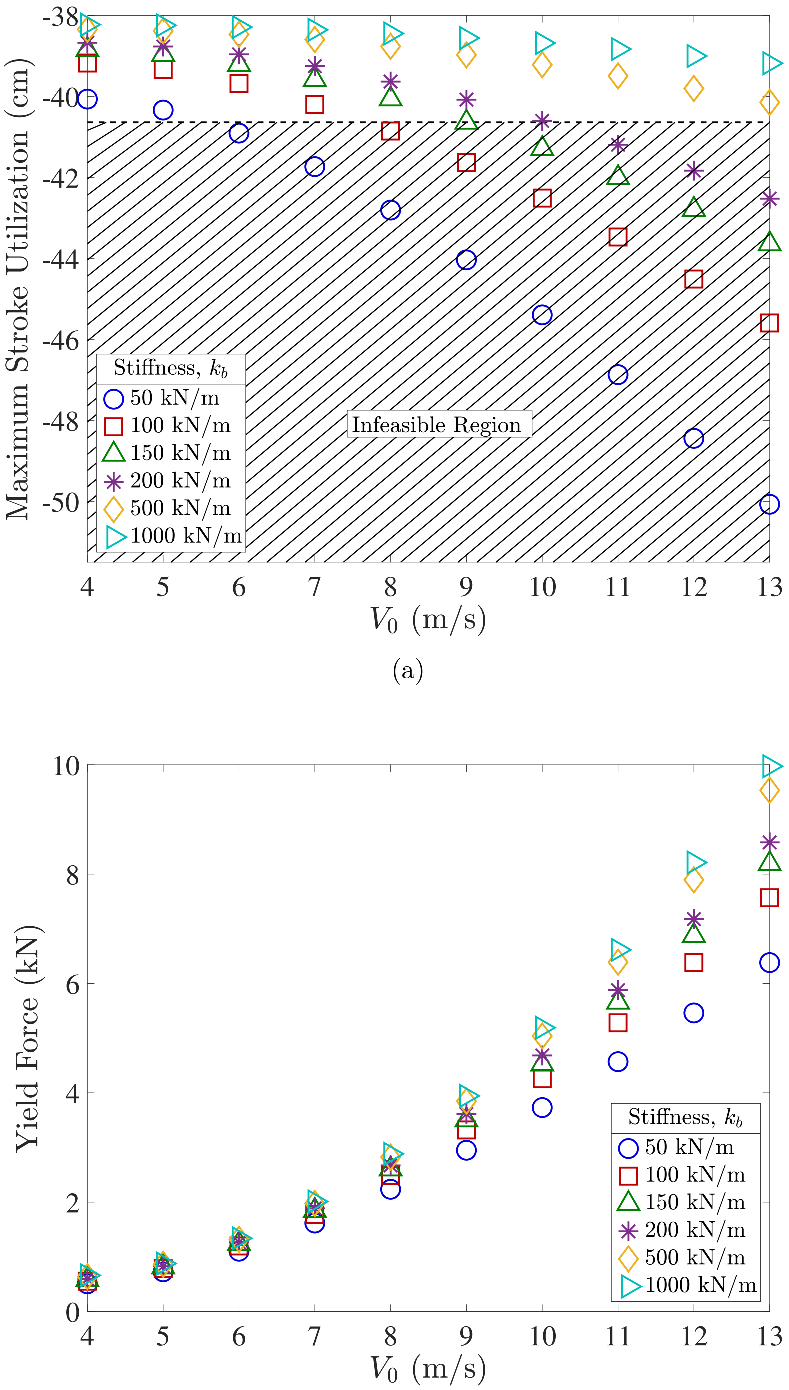

(a)

(b)

Figure 3.8: Stroke utilization and yield force results from parametric study of k_b

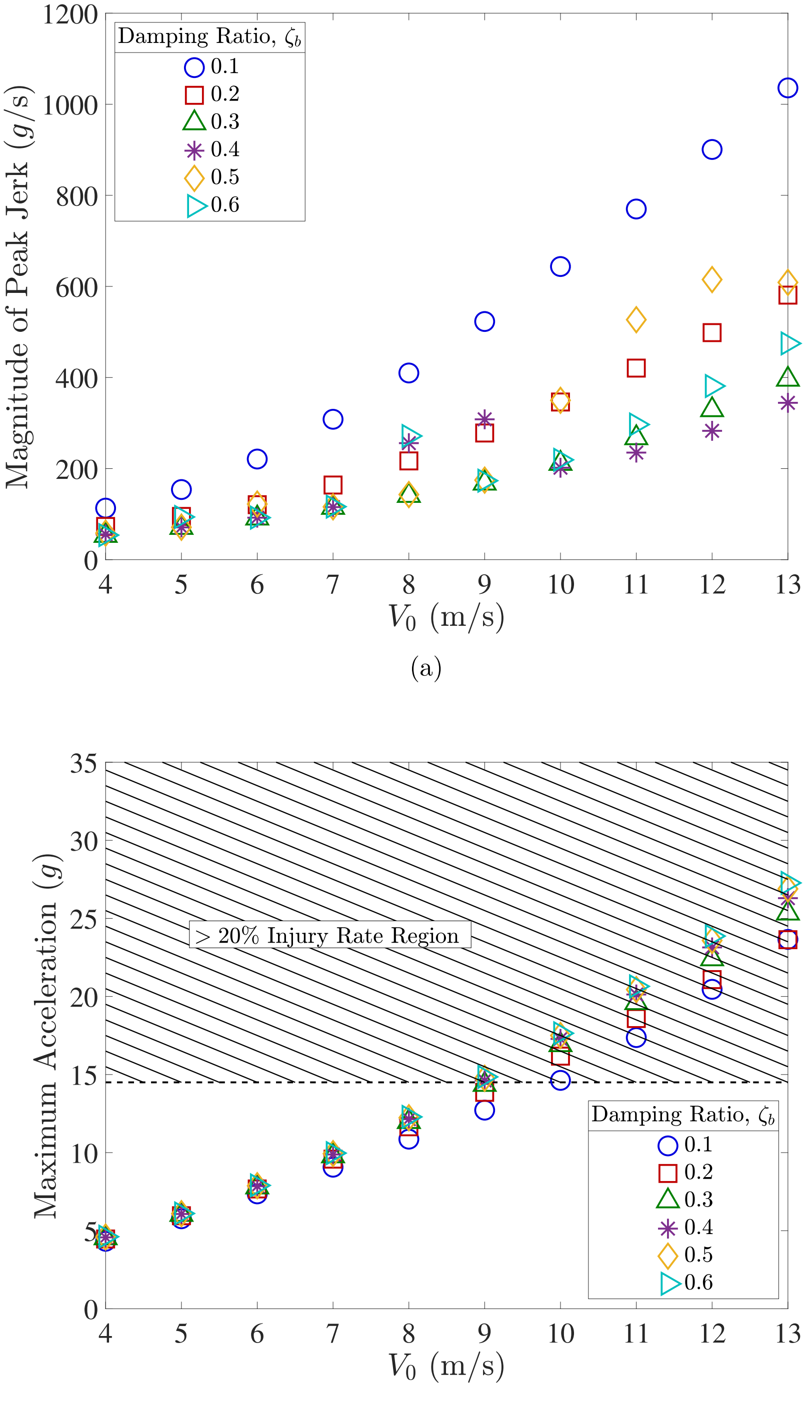

(a)

(b)

Figure 3.9: Jerk and peak acceleration results from parametric study of ζ_b

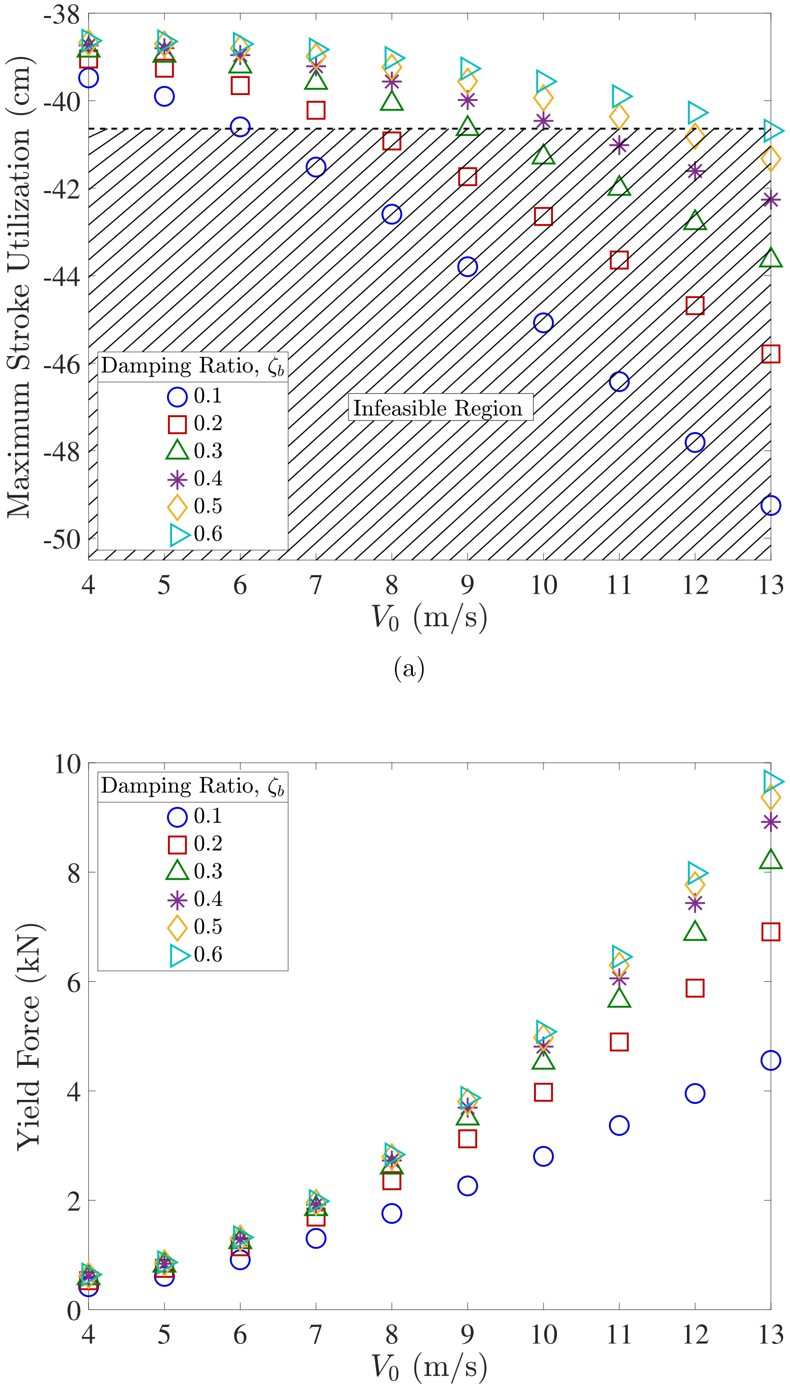

(a)

(b)

Figure 3.10: Stroke utilization and yield force results from parametric study of ζ_b

constraint, but those additional solutions will violate the 14.5 g limit load. Those solutions will also require higher yield forces.

Parameter Increased	$\max\lvert\dddot{x}\rvert$	$\max\lvert\ddot{x}\rvert$	Stroke Used	$f_{y,opt}$
k_b	↑	↑	↓	↑
ζ	–	↑	↓	↑

Table 3.4: Summary of Parametric Study Results

3.5 Effect of Occupant Weight

The effectiveness of YFO control applied to an MREA vertically stroking crew seat with a bumper is evaluated for the 5th percentile female and the 95th percentile male with weights of 47 and 97 kg respectively. The optimization scheme is run for both of these occupants with a seat in the baseline configuration ($c_m = 900$ Ns/m, $k_b = 150$ kN/m and $\zeta_b = 0.3$). Figures 3.11-3.14 plot the peak acceleration, stroke utilization, optimal yield force, and peak magnitude of the jerk determined using YFO control for each of these occupants over a V_0 range of 4-13 m/s. Similarly to the 10 m/s YFO control solution for the 50th male, the 7 m/s YFO control solution for the 5th female is adjusted to account for the stroke utilization trend. Table 3.5 details the array of initial drop velocities for which a feasible solution with a peak acceleration beneath the defined limit load exists. As it is used in this table, 'feasible solution' does not indicate the feasibility or convergence of the optimization but is considered in the same way as it was for SL control where a solution that did not exceed the maximum stroke was considered feasible. The convergence information is included in the last column of the table. Table 3.5 also lists the range of initial drop velocities for which the jerk is kept below 500 g/s. Comparing these results to those for SL control in Table 2.1, the range of feasible solutions which do not exceed the limit load for the 5th female is increased. The jerk is successfully kept under 500 g/s for the entire group of tested initial drop velocities for the 50th male and 95th male. The 5th female experiences peak magnitudes of jerk below 500 g/s for initial drop velocities of 5-11 m/s. Therefore, all feasible solutions with peak accelerations below 14.5 g also successfully minimize the jerk without introducing significant discontinuities in acceleration for the 50th male and 95th male.

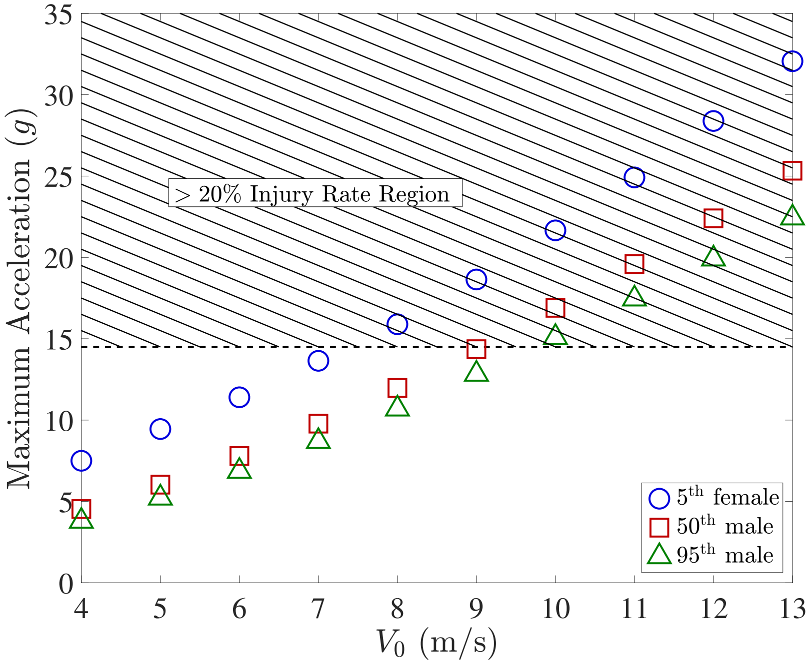

Figure 3.11: Peak accelerations using YFO control for all occupants

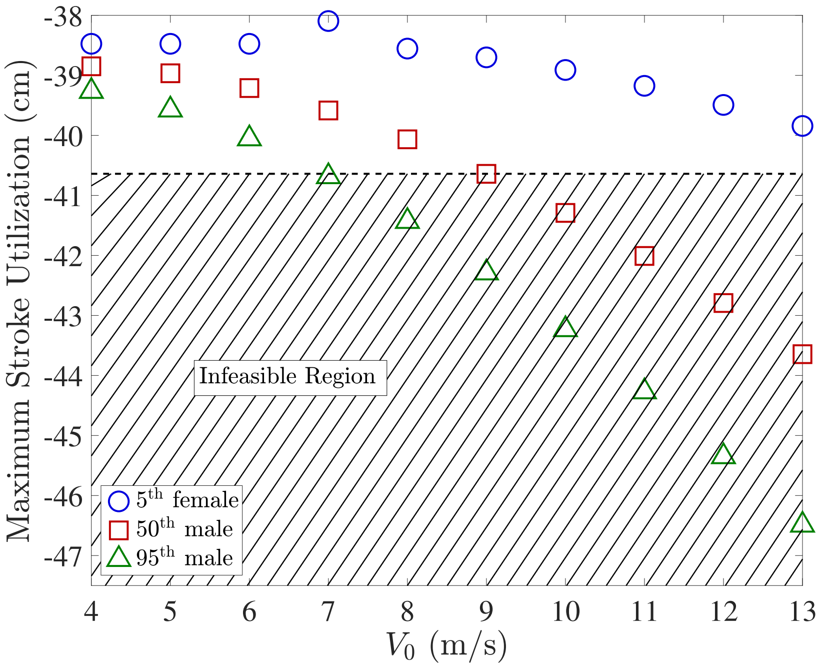

Figure 3.12: Stroke utilization using YFO control for all occupants

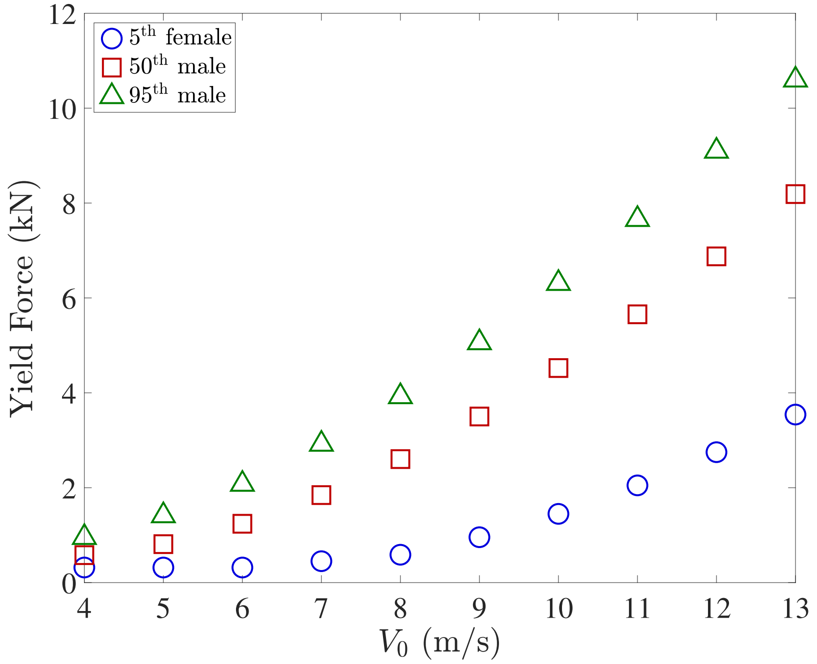

Figure 3.13: Yield forces using YFO control for all occupants

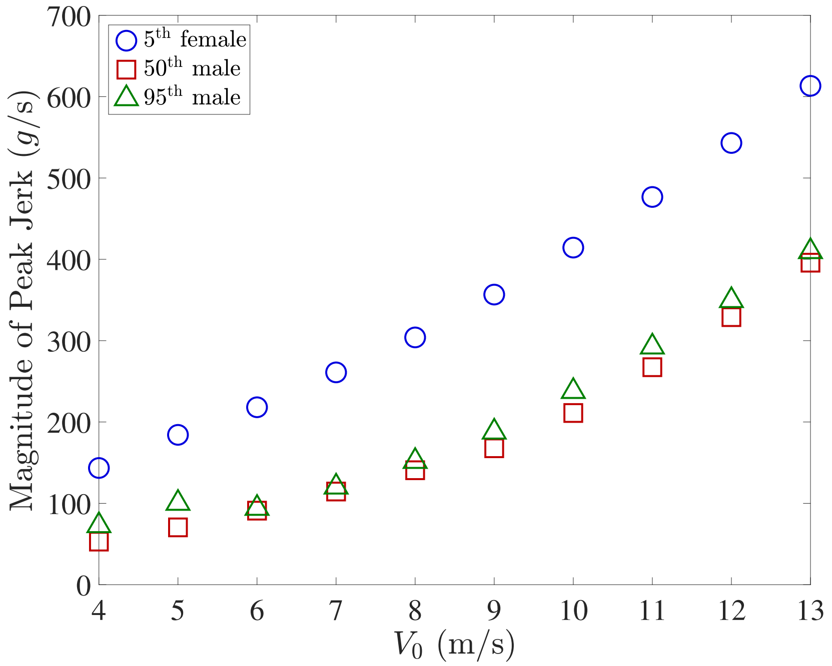

Figure 3.14: Peak jerk magnitude using YFO control for all occupants

Occupant	V_0 Range with a Feasible Solution Below 14.5 g	V_0 Range with Jerk Below 500 g/s	V_0 Range with Convergence
5th female	4-7 m/s	4-11 m/s	4-6, 8-13 m/s
50th male	4-9 m/s	4-13 m/s	4-9 m/s
95th male	4-7 m/s	4-13 m/s	4-7 m/s

Table 3.5: Range of Acceptable Solutions for Each Occupant

3.6 Conclusion

This simulation study provides a proof of concept that the addition of a bumper at the end of the stroke of an MREA can serve to bring the acceleration and jerk end levels down to zero. The bumper alone introduces a new discontinuity in acceleration when used in conjunction with the optimal yield force determined from SL control. This discontinuity in acceleration can be eliminated by optimizing the yield force to minimize the peak magnitude of the jerk while still bringing the velocity to zero and utilizing the majority of the stroke. When an MREA with a passive damping constant of $c_{MR} = 900$ Ns/m is used in conjunction with a bumper with $k_b = 150$ kN/m and $\zeta_b = 0.3$, the seat response can be kept within the 14.5g decelerative limit load and the maximum available 40.64 cm of stroke for a V_0 range of 4-9 m/s.

Overall, YFO control offers a more comprehensive definition of a 'soft landing' whereby the velocity, acceleration, and jerk are all brought down to zero while utilizing the majority of the stroke. It is evident that the implementation of YFO control is limited if the yield force is restricted to one value until contacting the bumper. Incorporation of other control strategies into the jerk minimization could result in more desirable solutions.

Chapter 4: The Effect of Mesocarbon Microbeads on the Behavior of Magnetorheological Fluid

4.1 Introduction

Chapters 2 and 3 demonstrate the effect of two potential MREA control algorithms on the dynamics of a vertically stroking crew seat undergoing an impact. These chapters are primarily concerned with the control algorithm and bumper properties, assuming that a fluid with the necessary capabilities is available. The capabilities required for the application of these control schemes to an MREA vertically stroking crew seat include a wide range of yield forces, fluid durability, minimal weight, and resistance to sedimentation. This chapter considers the use of nonmagnetizeable particles in MR fluid for enhancement of the yield force with a reduced weight penalty and endurance of the yield force properties.

A broad range of research has been conducted on the modification of MR fluids to meet desirable properties for practical applications. If limited to a basic MR fluid suspension of carbonyl iron particles (CIPs) in carrier fluid, the modifications which can be made to the fluid are limited in scope. In general, one can modify the volume percent (vol %) and size of the magnetizeable particles and the type of carrier fluid itself (e.g. a carrier fluid with a different viscosity may be chosen). However, if additives and other nonmagnetizeable particles are introduced into the MR fluid, the potential modifications are innumerable, ranging from the addition of fumed silica to decrease sedimentation rate [25] to adding nonmagnetizeable particles to enhance the MR fluid's response to a magnetic field [6, 26, 43, 44]. This chapter builds upon previous work in the area of MR fluid yield force enhancement via nonmagnetizeable particles.

4.1.1 Previous Work

Recent studies have sought to maximize the capabilities of MR fluid by increasing τ_y or f_y, thereby widening the range of forces or stresses at which the fluid can operate. One method of increasing the yield properties of MR fluids is by adding passive particles, here defined as particles with no magnetization or much lower magnetization than carbonyl iron, to the fluid.

Both simulations and experiments show augmentation of the MR effect in fluids employing passive particles [6,26,43,44]. The simulation studies of [26] and [44] show an increase in MR fluid yield stress with increasing passive particle volume fraction for a constant magnetizeable particle volume fraction. This yield stress enhancement has been attributed to a particle jamming-like mechanism via which repulsive clusters form including magnetizeable and nonmagnetizeable particles of the same average diameter [44]. The results of these simulations are validated in experimental studies. Ulicny et al. showed that increasing the volume fraction of hollow glass beads while maintaining a constant volume fraction of carbonyl iron particles resulted in an increasing fluid yield stress at magnetic saturation [26]. Powell et al. found that the substitution of hollow glass spheres for a fraction of the iron particles produced an initial doubling of the yield force [6]. However, it was also found that when the fluids were subjected to endurance tests, the high yield force of the fluid with passive particles dropped back down to the yield force level of the fluid without passive particles [6]. SEM images revealed no glass beads in the fluid after the completion of endurance testing, suggesting that the yield force drop was due to the glass beads being crushed [6].

The objective of this study is thus to find a particle which similarly augments the dynamic capabilities of the MR fluid, while withstanding endurance testing. Mesocarbon microbeads (MCMBs) are chosen as potential yield force-enhancing passive particles with increased durability. The MCMBs are of a similar size to the glass beads used in [26] and [6], but, whereas the glass beads were hollow, the MCMBs are solid. Based on the previous study by [6] and the study by [44], the combination of MCMBS and CIPs, should result in a fluid synergistically combining the MR effect and particle jamming.

4.2 Background Material

MR fluids are part of a group of fluids characterized by an individual yield stress, τ_y. Below a given fluid's yield stress, the fluid is in the preyield region and will exhibit rigid behavior [45]. At and above its yield stress, the fluid is in the postyield region and will exhibit viscous flow [45]. The yield stress can thus be thought of as the minimum stress required for the fluid to flow. The Herschel-Bulkley (HB) model, which modifies the equation of a power law fluid, has been used as a constitutive model for MR fluids [46]:

$$\tau = \tau_y + K(\dot{\gamma})^n \tag{4.1}$$

where τ_y is the yield stress, K is the consistency, $\dot{\gamma}$ is the shear rate, and n is the flow index. When $n = 1$, the HB model reduces to the linear Bingham plastic (BP) model [46]. Alternatively, when $n > 1$, the fluid exhibits shear thickening and when $n < 1$, the fluid exhibits shear thinning [46]. These three cases of the HB model are shown in Figure 4.1.

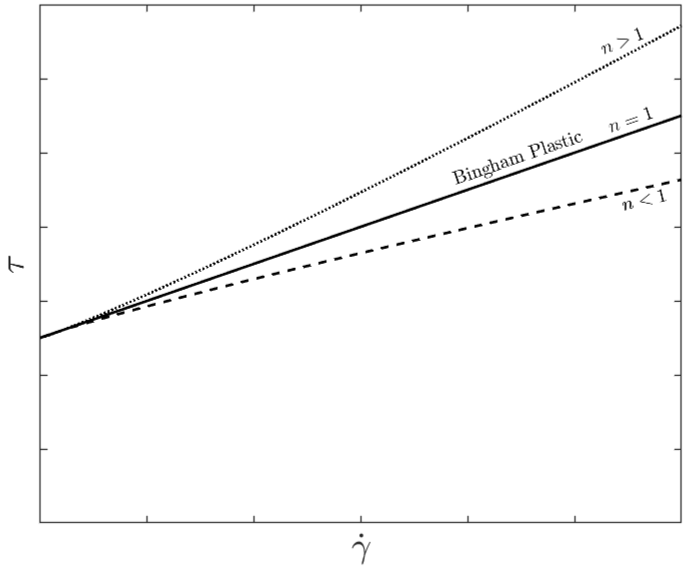

Figure 4.1: Herschel-Bulkley model

The shear stress versus shear rate data for a fluid are referred to as the fluid's flow curve. For magnetorheological fluids, the BP model is well-suited to the high shear rate portions of the flow curves, where the shear stress and shear rate take on a more linear relationship [6, 45, 47]. The HB model is better suited to capture the flow curve trends over a wider range of shear rates [46]. Studies using the BP model address the issue of the low shear rate region by either only implementing the model above a given shear rate [6, 45] where the activity of the curve is linear or using a weighted-least-squares error fit where the higher shear rates are given a higher weight [47]. This work will examine the activity of the fluids at high shear rates using the BP model.

4.3 Methodology

Six MR fluids with an iron particle volume fraction, ϕ_{Fe}, of either 0.35 or 0.40 and a carbon particle volume fraction, ϕ_C, of 0, 0.05, or 0.10 were formulated and tested in shear mode and in flow mode.

4.3.1 Fluid Formulation

MIL-PRF-83282D (AeroShell Fluid 31; Shell), a synthetic hydrocarbon hydraulic fluid with a kinematic viscosty of 14.0 mm^2/s at 40° C was used as the carrier fluid. MIL-PRF-83282D is commonly used in aircraft applications and has a comparable viscosity to the fluid used in a previous study employing glass beads as passive particles. It is thus a carrier fluid with viable practical applications that can be compared to past experimental work. The carbonyl iron particles (BASF) were added in a bidisperse mixture (1:1 ratio of 1.8-2.3 μm and 7-9.5 μm average diameter CIPs). The appropriate volume percent (0, 5, or 10 vol%) of MCMBs (Bonding Chemical, 10-13 μm average diameter) was added. All fluid compositions are listed in Table 4.1.

Sample Name	MIL-PRF-83282D [vol%]	CIPs [vol %]	MCMBs [vol %]
MR-Fe35-C0	65	35	0
MR-Fe35-C5	60	35	5
MR-Fe35-C10	55	35	10
MR-Fe40-C0	60	40	0
MR-Fe40-C5	55	40	5
MR-Fe40-C10	50	40	10

Table 4.1: MR Fluid Compositions

4.3.2 Rheometer Tests

The rheological properties of all fluids were tested in shear mode via an Anton-Paar, Paar Physica MCR 300 parallel plate rheometer outfitted with an MRD 180 magnetorheological cell (see Figure 4.2(a)). During these tests, the shear rate was varied from 0.1-1000 s^{-1}. The shear stress (τ) versus shear rate ($\dot{\gamma}$) flow curves are used to determine the off-state viscosity and a range of yield forces for each fluid. The viscosity is measured using a 0.15 mL sample and 0.5 mm fluid gap when no magnetic field is applied and the yield stresses are determined using 0.3 mL samples and a 1 mm fluid gap while applying induced magnetic fields due to currents ranging from 0.2-5 A (induced magnetic field strength of 31-554.6 mT). Although the conversion from current to magnetic field strength is available for the rheometer, similar data is not available for the damper used. Thus, all results are presented in terms of current.

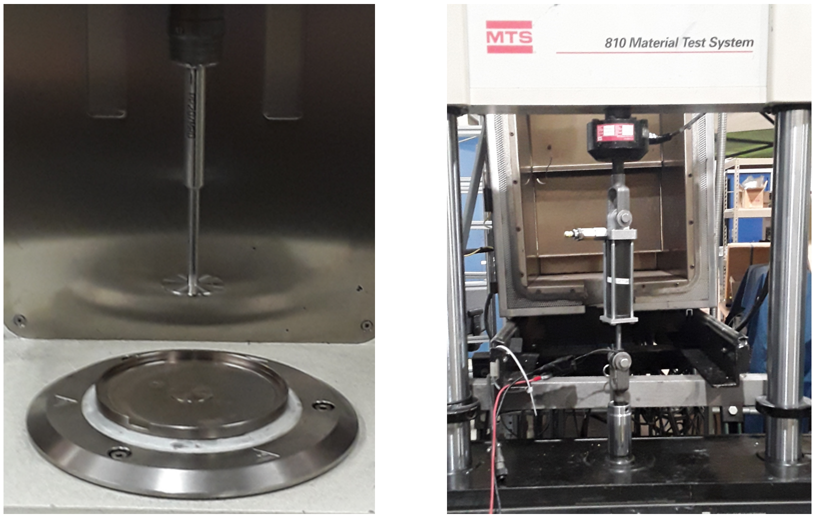
(a) (b)

Figure 4.2: (a) Rheometer and (b) MR damper mounted on MTS machine

4.3.3 Damper Tests

The fluids were tested in flow mode using a modified RD-8041-1 long stroke MR damper (LORD Corporation). The damper was mounted on a Material Test System (MTS) 810 machine and pressurized to 2000 kPa (300 psi). The damper piston was compressed by 19.05 mm (0.75 in) and cycled via a 1 Hz sinusoidal excitation with ± 12.7 mm (0.5 in) of stroke. Force and displacement data were taken at currents ranging from 0-1 A in 0.2 A increments. This data was then used to obtain yield forces. At 1 A, the fluids approach magnetic saturation. Figure 4.2(b) shows the damper on the MTS machine.

4.3.4 Endurance Tests

The endurance of the MCMBs in MR fluids was investigated by testing a representative fluid, MR-Fe40-C5, in the MR damper and cycling the piston with a 2 Hz sinusoidal excitation and no applied current. Every 10,000 cycles, the procedure in Section 4.3.3 was repeated: the piston was cycled with a 1 Hz sinusoidal excitation and yield forces were obtained for applied currents ranging from 0-1 A. This was repeated until 100,000 cycles at the 2 Hz cycling frequency were completed. The higher frequency, longer duration cycling of the damper with multiple on-state testing sequences introduces challenges to the experimental setup. In initial endurance testing of one fluid in the damper up to 25,000 cycles, a significant increase in temperature was observed. There was also visible flexing of the test fixture. To reduce temperature effects, the cooling system shown in Figure 4.3 was introduced whereby chilled water was circulated through copper tubes encircling the damper. To effectively cool the damper, the copper tubes must be in contact with the damper body, requiring adequate clearance between the damper body and the threaded rods used to seal the damper. An updated fixture was thus designed to accommodate the necessary clearances. The material was also changed from aluminum to stainless steel in an effort to provide increased resistance to flexing. A model of the fixture is shown in Figure 4.4.

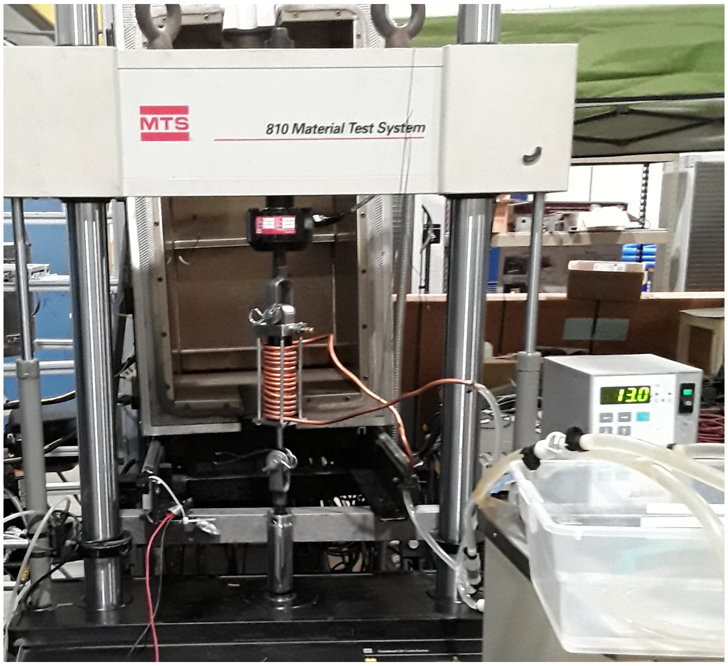

Figure 4.3: Cooling system

(a)

(b)

Figure 4.4: Modified (a) bottom and (b) top damper fixtures

4.4 Results

This section details the results of the rheometer, damper, and endurance testing of the fluids.

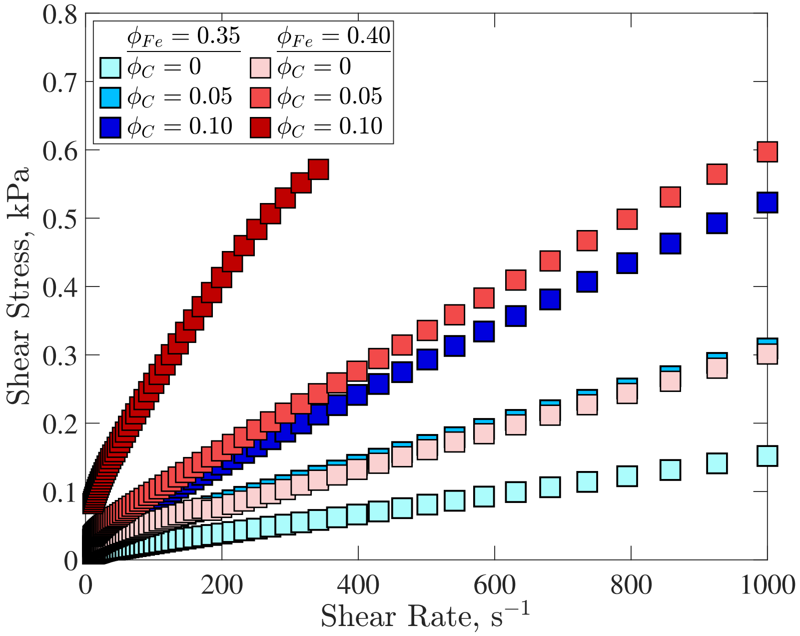

Figure 4.5: Example rheometer data with the magnetic field off

4.4.1 Rheometer Testing

Figure 4.5 displays the flow curves resulting from the field off rheometer tests. The blue curves represent fluids with $\phi_{Fe} = 0.35$ and the red curves correspond to fluids with $\phi_{Fe} = 0.40$. The darker shades in each color scheme indicate higher ϕ_C and lighter shades indicate lower ϕ_C. The slope of each flow curve gives the fluid's viscosity (μ). As expected, fluid viscosity increases with increasing total particle volume fraction, ϕ_p, and particles with the same ϕ_p have similar viscosities. For the fluids with $\phi_{Fe} = 0.35$, the viscosities of the fluids are 0.14 Pa-s, 0.30 Pa-s, and 0.52 Pa-s for $\phi_C = 0$, 0.05, and 0.10 respectively. For the fluids with $\phi_{Fe} = 0.40$, the viscosities of the fluids are 0.30 Pa-s, 0.54 Pa-s, and 1.55 Pa-s for $\phi_C = 0$, 0.05, and 0.10 respectively. The fluid with the highest total particle volume fraction is only shown up to 400 s^{-1} because the shear stress begins to drop off after that point.

Figure 4.6 shows example rheometer data when the magnetic field is on for five input currents (corresponding to five magnetic field strengths). As outlined in Section 4.2, the Bingham plastic model correlates the most closely with high shear rate flow curves [6, 45, 47]. Thus, the flow curves from the field on tests are fitted from 300-1000 s^{-1} with the BP model:

$$\tau = \tau_y + \mu\dot{\gamma} \tag{4.2}$$

where τ_y is the yield stress, μ is the viscosity, and $\dot{\gamma}$ is the shear rate. These high shear rate fit lines are represented with the black dashed lines in Figure 4.6 where the y-axis intercept indicates the yield stress. Figure 4.7 shows yield stress as a function of the current applied for all six fluids. While each of the fluid curves shows a similar trend, no correlation between the calculated yield stresses and the volume fraction of MCMBs is evident. The yield stress curves in Figure 4.7 do show a decreasing slope with increased current after 2.5 A. After this input current, the yield stress begins to stabilize, approaching magnetic saturation, defined as increasing current with no further increase in stress. The six fluids approach magnetic saturation within the range of 4-5 A, corresponding to an induced magnetic field range of 505-554.6 mT.

Figure 4.8 shows an example of an MR sample with MCMBs after rheometer testing with the field on and off. The color distribution in the fluid samples after the rheometer tests suggests a migration of the darker carbon particles: to the center for the field off tests (Figure 4.8(a)) and to the edges for the field on tests (Figure 4.8(b)). In the field off case, the centripetal force on the fluid likely causes the

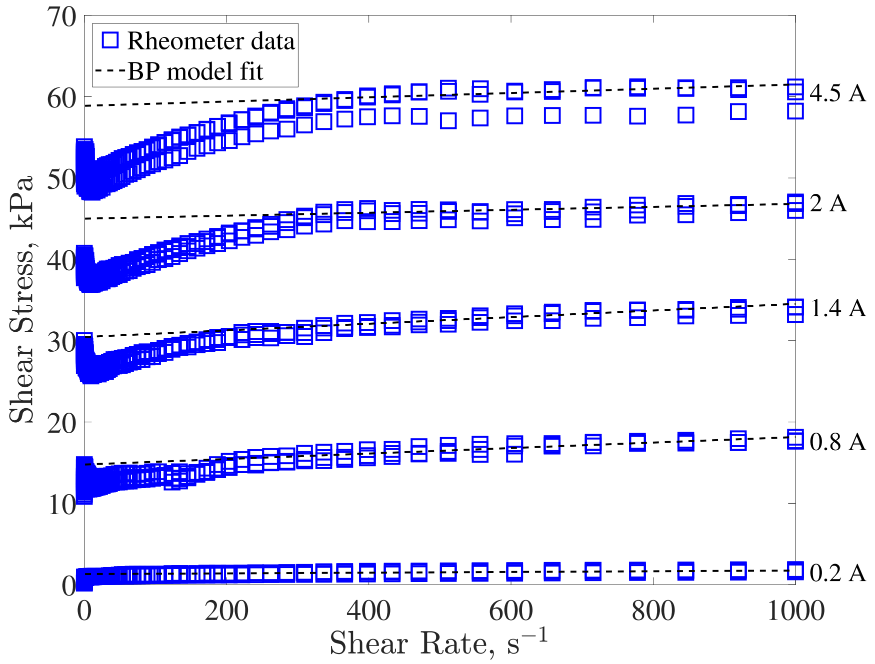

Figure 4.6: Example field on rheometer data and Bingham Plastic model fit

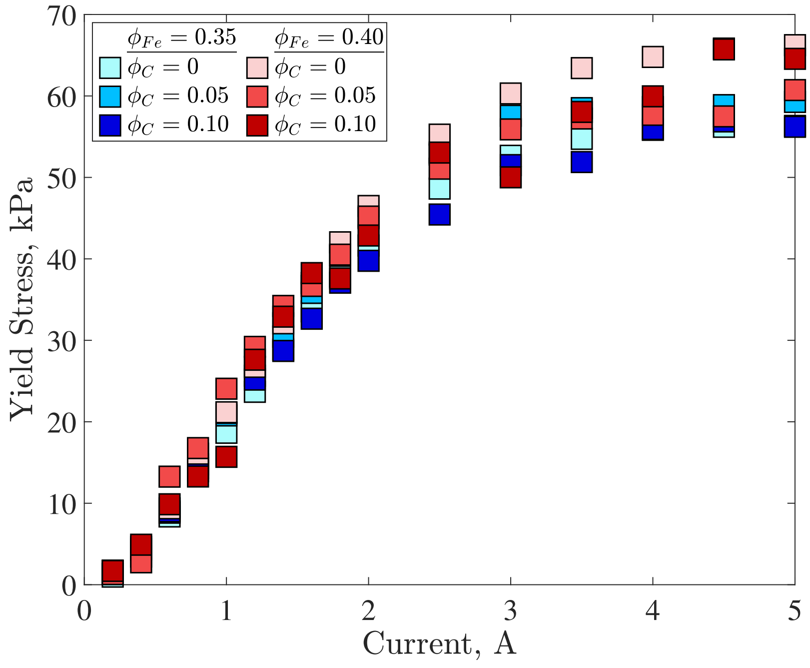

Figure 4.7: Rheometer data with the magnetic field on


(a) (b)

Figure 4.8: Fluid after rheometer testing with (a) the field off (b) the field on

inward movement of the lower density MCMBs. In the field on case, it is common for some carrier fluid to leak out of the gap between the two rheometer plates, while the iron particles remain in the particle chains. The darker outer ring present in Figure 4.8(b) is therefore likely due to fluid containing MCMBs leaking out of the gap. The visible separation of the carrier fluid and the MCMBs from the CIPs provides a feasible explanation for why there is no distinct relationship between MCMB concentration and yield stress in the shear mode test results.

4.4.2 Damper Tests

The lack of correlation between yield stress and carbon volume fraction reinforces the necessity of testing the fluids in flow mode. The force and displacement data from the MTS machine tests of the MR damper are shown in Figure 4.9(a) and displayed as force vs. velocity curves in Figure 4.9(b). The force vs. velocity curves are fitted with the Bingham plastic damper force model:

$$F(t) = F_y sgn(\dot{x}) + C_{po}\dot{x} \tag{4.3}$$

where $F(t)$ is the force applied to the damper piston, F_y is the yield force, C_{po} is the post-yield damping constant, and $\dot{x}$ is the velocity. If the data is asymmetric in terms of force, the force must be centered around zero as in Figures 4.9(a) and 4.9(b) before fitting the Bingham plastic model. In Figure 4.9(b), F_y is the magnitude of the y-axis intercepts of the dashed model lines.

Figure 4.10(a) displays the yield force for each fluid composition as a function of damper input current. Two phenomena are present: 1) the MR effect whereby the yield force increases due to increasing ϕ_{Fe} and to increasing current and 2) the MCMB effect whereby the yield force is a nonlinear increasing function of ϕ_C. While the MR effect is present in all MR fluids and is independent of passive particle content, the MCMB effect is unique to this study and reinforces the phenomena observed by adding other passive particles to MR fluids. In Figure 4.10(a), the passive force required to move the piston when no current is applied is similar for all six fluids. Once a current is applied, however, the resulting yield forces separate. The fluid with $\phi_{Fe} = 0.35$ and $\phi_C = 0.10$ aligns with the curve for the fluid with $\phi_{Fe} = 0.40$ and $\phi_C = 0$, indicating that an additional 10 vol% of carbon beads has a similar effect to an additional 5 vol% of iron particles. The MCMB effect is greatest in the fluid with $\phi_{Fe} = 0.40$ and $\phi_C = 0.10$ at a current of 1.0 A. Overall, the results indicate that MCMBs enhance the yield force effect produced by the CIPs. Furthermore, as seen in the rheometer on-state testing results, the fluids

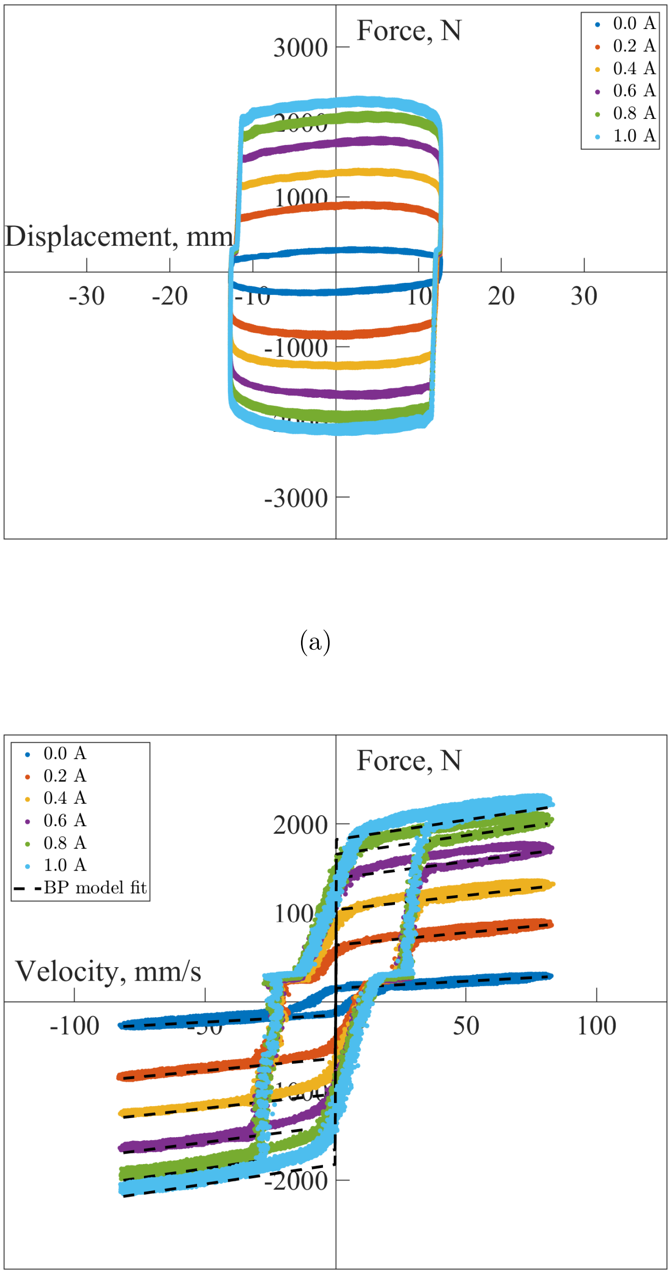

(a)

(b)

Figure 4.9: Results of the dynamic testing of the MR fluids in an MR damper using the MTS machine: (a) example displacement plot for one fluid and (b) example velocity plot for one fluid

approach magnetic saturation with increased current. While fluids in the rheometer reached magnetic saturation within the 4-5 A range, fluids in the damper approach saturation levels at 1 A. Therefore, the 1 A damper input current should correspond to a magnetic field strength within the range of 475.8-531.1 mT (3.5-4.5 A input current in the rheometer). This study has thus examined the six fluids in shear and flow modes within the ideal working range of MR fluids which is below levels approaching magnetic saturation.

To further evaluate the magnitude of the effect of the MCMBs on the MR fluids, a yield force percent change due to the addition of the carbon particles can be defined as follows:

$$F_y \text{ \% change} = \frac{F_y(\phi_C = x) - F_y(\phi_C = 0)}{F_y(\phi_C = 0)} \qquad (4.4)$$

$$\text{where } x = 0.05, 0.10$$

Figure 4.10(b) , shows the yield force percent change for a 5 or 10 vol% change in particles as a function of the current, with the dashed lines giving the average enhancement for a particular fluid across all currents. It is evident that the yield force percent change increases with increasing ϕ_C and with increasing ϕ_{Fe}. For the available fluids, the yield force percent change ranges from 10.6-66.8% and remains relatively constant across varying current levels. An average yield force percent change of 60.6% occurs when ϕ_C is increased from 0 to 0.10 for fluids with $\phi_{Fe} = 0.40$. This is more than double the 22.7% average yield force percent change that results from increasing ϕ_C from 0 to 0.05 for the fluid with $\phi_{Fe} = 0.40$, again portraying the nonlinearity of the MCMB effect. This is also true when comparing the yield force percent change for a 0.05 versus 0.10 increase in ϕ_C with $\phi_{Fe} = 0.35$.

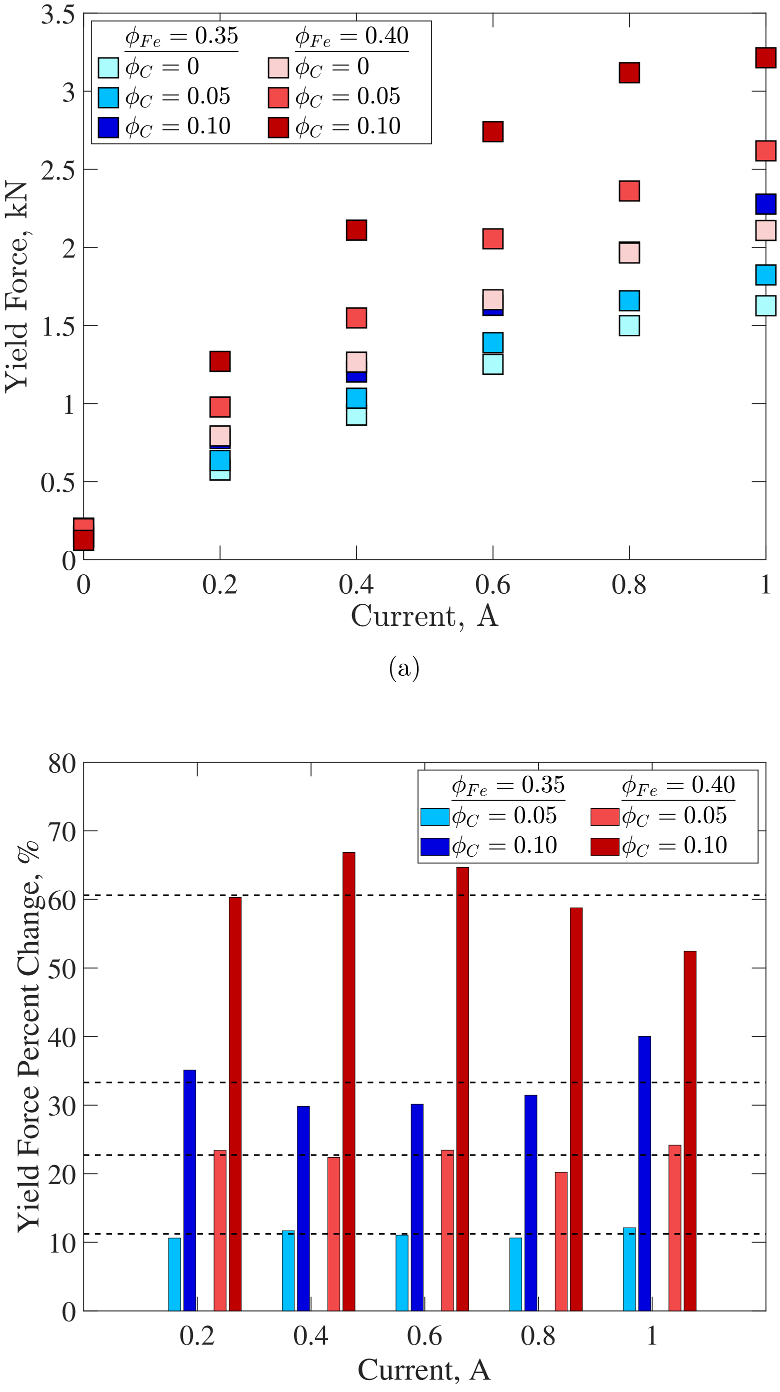

(a)

(b)

Figure 4.10: (a) Yield Force as a Function of Current for All Fluids and (b) Yield Force Percent Change

4.4.3 Weight Analysis

It is apparent that increasing either ϕ_C or ϕ_{Fe} increases the yield force of an MR fluid. While the yield force enhancement due to increasing the CIP volume fraction from 0.35 to 0.40 is higher than the enhancement due to increasing the MCMB volume fraction from 0 to 0.05 or from 0.05 to 0.1, it is necessary to consider the additional weight required for the yield force enhancement, thereby providing a measure of the enhancement efficiency of each particle. To evaluate the yield force enhancement efficiency, this study considers the two cases among the six fluids where there exists one fluid composition, referred to as the 'baseline', a second fluid with $\Delta\phi_C = 0.05$ from the baseline, and a third fluid with $\Delta\phi_{Fe} = 0.05$ from the baseline (see Figure 4.11). The first case considered is baseline fluid MR-Fe35-C0 for which a 5 vol% increase in CIPs is achieved with MR-Fe40-C0 and a 5 vol % increase in MCMBs is reached by MR-Fe35-C5. Similarly, the second case considered is baseline fluid MR-Fe35-C5 for which a 5 vol% increase in CIPs is reached by MR-Fe40-C5 and a 5 vol % increase in MCMBs is achieved with MR-Fe35-C10. Considering these two cases, a yield force coefficient is defined as

$$\text{yield force coefficient} = \frac{\Delta F_y}{\Delta mg} \tag{4.5}$$

where ΔF_y is the difference between the yield force of a fluid with a 5 vol% increase in particles and the yield force of the baseline fluid $(F_{y,new} - F_{y,baseline})$ at a given current and Δmg is the additional weight due to the increase in ϕ_C or ϕ_{Fe}. A 100 mL volume of fluid is assumed for the yield force coefficient calculation. The weight

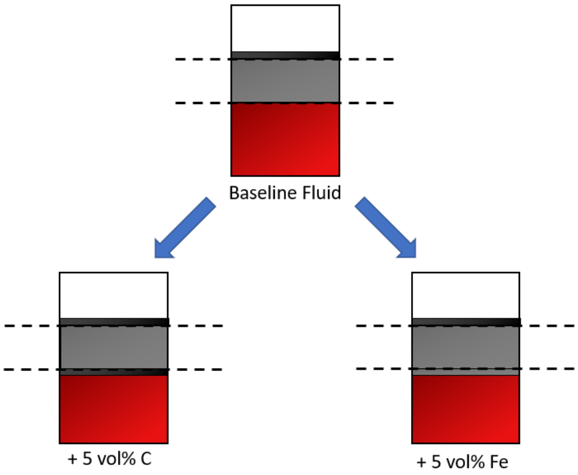

Figure 4.11: 5 vol % change in fluid composition

change, Δmg, in a 100 mL fluid is always 10.90 g for an additional 5 vol% of MCMBs and 39.35 g for an additional 5 vol% of CIPs.

Figure 4.12 displays the yield force coefficients for each case at all of the nonzero applied currents. Figure 4.12(a) shows the results for the baseline fluid MR-Fe35-C0 and Figure 4.12(b) gives the results for baseline fluid MR-Fe35-C5. The black bars indicate a 5 vol% increase in MCMBs while the grey bars indicate a 5 vol% increase in CIPs. With the exception of the yield force coefficient at 0.2 A for the MR-Fe35-C0 baseline fluid, the yield force coefficient for a 5 vol% of MCMBs is always higher than the yield force coefficient for a 5 vol% increase of CIPs. The difference in yield force coefficient increases generally with increasing current and increasing initial MCMB volume fraction. For the MR-Fe35-C5 baseline fluid, the yield force coefficient for a 5 vol% increase in MCMBs at 1 A is more than double the yield force coefficient for a 5 vol% increase in CIPs. As a whole, the results indicate that the same additional weight of carbon beads instead of iron particles

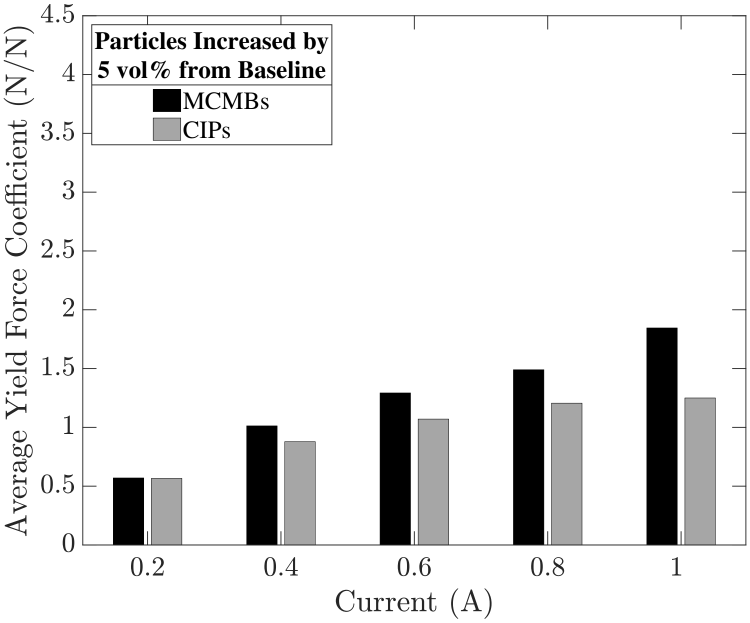

(a)

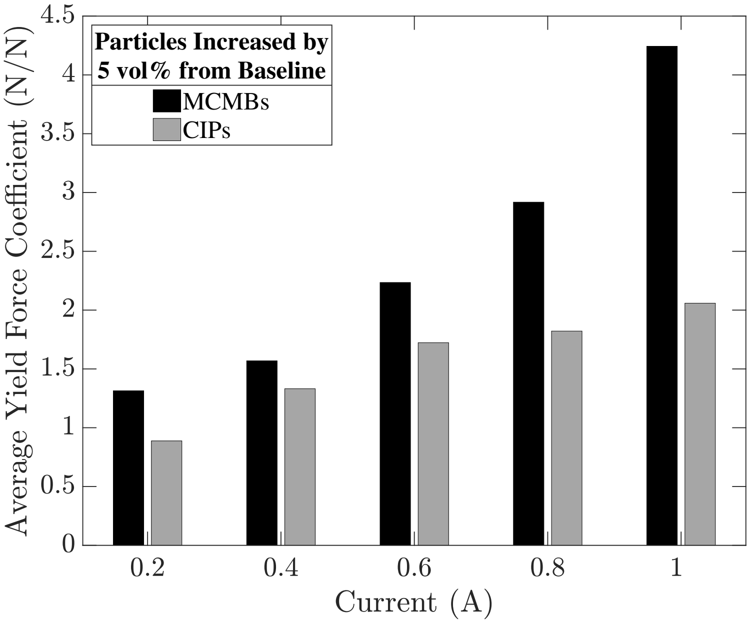

(b)

Figure 4.12: Yield force coefficients for a 5 vol % change in MCMBs or CIPs from baseline fluids of (a) MR-Fe35-C0 and (b) MR-Fe35-C5

will result in a higher yield force. The MCMBs thus offer weight savings desirable for many MR fluid applications.

Furthermore, the yield force coefficients seen in Figure 4.12 increase nonlinearly with respect to the baseline fluid composition. Adding MCMBs when there is already a total particle volume fraction of $\phi_p = 0.40$ has more of an effect than if the baseline fluid has a ϕ_p of 0.35. This phenomenon indicates that a mechanism similar to the particle jamming-like one described in [44] may be causing the increase in yield force.

4.4.4 Endurance Testing

Figure 4.13 displays the results of yield force tests of MR-Fe40-C5 over a period of 100,000 cycles, corresponding to 5,080,000 mm, or approximately 5 km, of piston travel. For input currents of 0.2-1 A, there is no appreciable drop in yield force over 100,000 cycles. The black vertical lines in the plot delineate pauses between test days. The fluid changing overnight could be a potential contributor to the jumps in yield force. After 100,000 cycles were completed, the presence of a visible cake was evident in the piston, suggesting that particle aggregation was occurring (see Figure 4.14).

A comparison of the durability of the MCMBs and of the glass beads is presented in Figure 4.15 by adapting the 1 A endurance testing results of [6] and of the current study. Yield force is plotted in terms of piston travel for both studies. Figure 4.15(a) shows the yield force decay of MRF-37, an MR fluid composed of

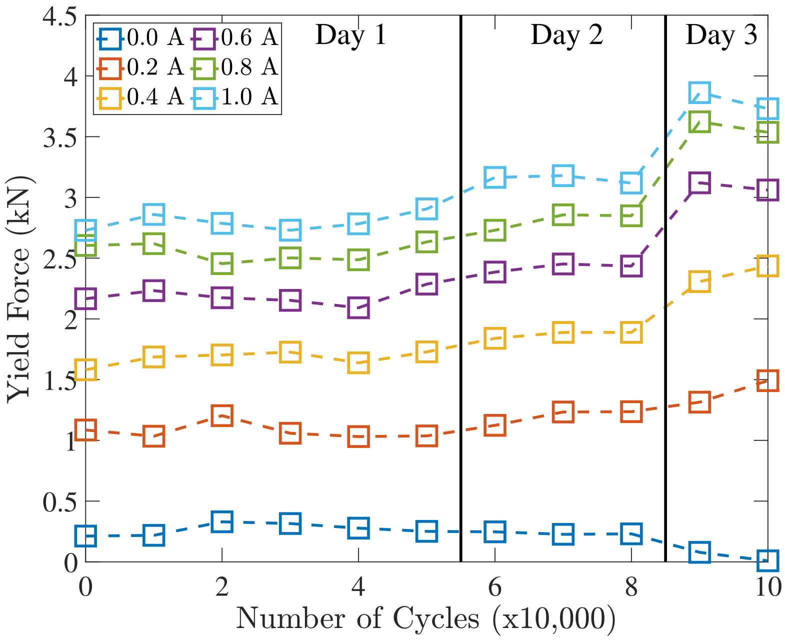

Figure 4.13: Yield force of MR-Fe40-C5 at six input currents over 100,000 cycles

Figure 4.14: Damper and piston after endurance testing

37.5 vol% CIPs, 4.3 vol% glass beads, and 60 vol % carrier fluid [6]. The drop in yield force is consistent and continues until the piston has traveled 4.6 km, after which the yield force levels off at nominally 180 N, less than half of the initial yield force. This plateau point is labeled “glass bead failure”. Conversely, the fluid

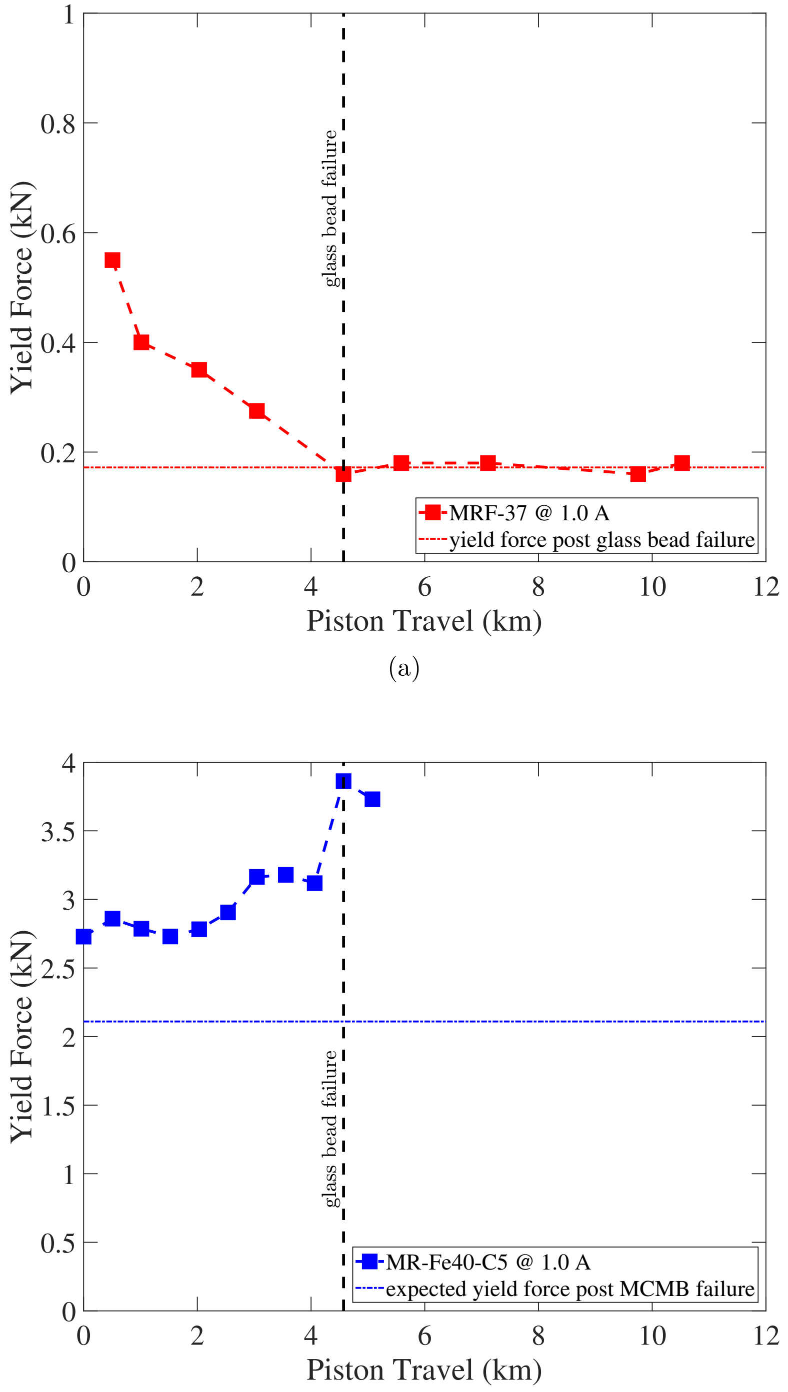

(a)

(b)

Figure 4.15: Endurance testing results taken at an input current of 1.0 A for (a) data adapted from [6] and (b) the current work

with MCMBs in Figure 4.15(b) remains relatively stable at nominally 2750 N for 2.5 km of piston travel on the first day of testing. On the second day of testing the yield force maintains a relatively stable average of 3150 N. On the third day of piston travel, there is the aforementioned jump in yield force. Overall, the fluid with MCMBs maintains its yield force-enhancing properties longer than the fluid with glass beads which shows immediate degradation, suggesting that the MCMBs are a more durable option for use in MR fluids.

4.5 Nondimensional Plug Thickness

The theoretical nondimensional plug thickness can provide insight into the mechanism via which the MCMBs increase the yield force of an MR fluid [48, 49]. Wereley and Pang analyze a flow mode damper using approximate parallel plate models [49]. This analysis assumes a basic fluid element with a velocity profile divided into three regions: one pre-yield and two post-yield (see Figure 4.16). The shear stress in the pre-yield region is less than the yield stress, meaning that the iron particle chains remain in tact and the fluid behaves like a solid with a thickness of δ. This region is referred to as the "plug". The fluid in the post-yield regions experiences shear stresses higher than the yield stress, and so behaves like a fluid.

The thickness of the pre-yield plug, δ, can be nondimensionalized by the thickness of the gap, d, and related to the ratio of the damping constant with the field on and off by [49]:

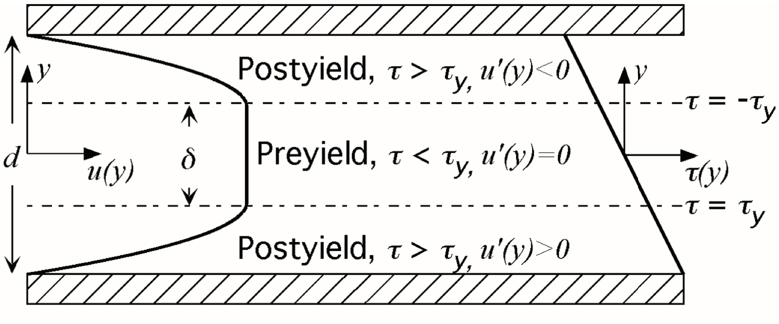

Figure 4.16: Velocity profile of a flow mode damper fluid element from [7]

$$\left(\frac{C_{eq}}{C}\right)_f = \frac{1}{(1-\bar{\delta})^2(1+\bar{\delta}/2)} \tag{4.6}$$

where $\bar{\delta}$ is the nondimensional plug thickness, $C_{eq,f}$ is the equivalent viscous damping constant, and C_f is the Newtonian damping constant. Using $F = C_{eq,f}v_0$ and solving for $\bar{\delta}$, yields

$$\frac{1}{2}\bar{\delta}^3 - \frac{3}{2}\bar{\delta} + 1 = \frac{F_0}{F_y} \tag{4.7}$$

where, for any given fluid, F_0 is the force with the field off and F_y is the yield force measured at a defined current. Using the results of the damper tests to obtain the force ratios, the nondimensional plug thicknesses due to currents ranging from 0.2-1 A can be solved for using MATLAB's `fsolve` command. The resulting force ratio as a function of nondimensional plug thickness is plotted in Figure 4.17(a).

The direction of increasing current for each fluid is from left to right on the plot. For each ϕ_{Fe}, as ϕ_C is increased, the points move farther along the curve (i.e. the plug thickness at a given current is higher when there is more carbon in the suspension). The increase in plug thickness is higher when going from $\phi_C = 0.05$ to $\phi_C = 0.10$ than when going from $\phi_C = 0$ to $\phi_C = 0.05$. Figure 4.17(b) further breaks

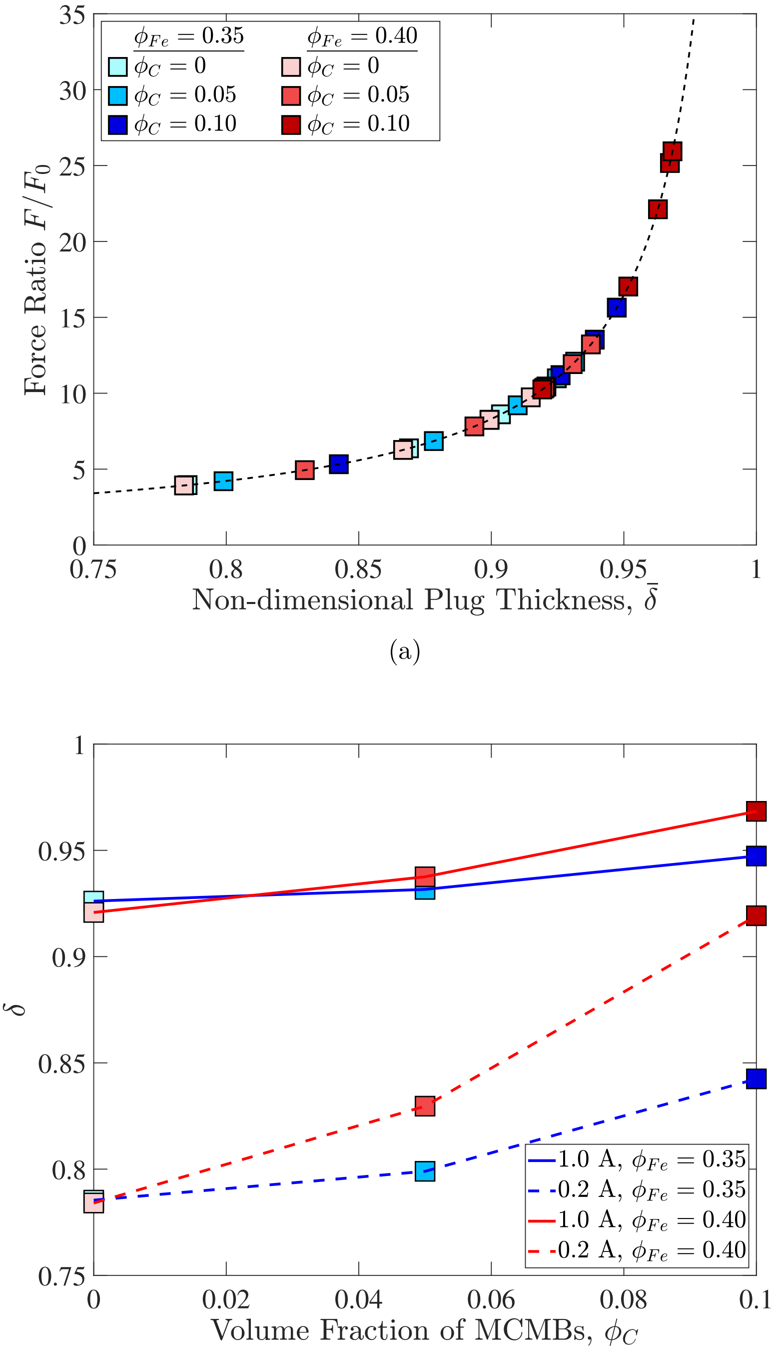

(a)

(b)

Figure 4.17: (a) Force ratio as a function of nondimensional plug thickness for all fluids and (b) nondimensional plug thickness as a function of fluid composition at 0.2 A and 1.0 A

down the relationship between plug thickness and fluid composition. For clarity, only the minimum and maximum current cases are displayed. As the percentage of carbon by volume is increased, $\bar{\delta}$ increases. The increase is more substantial for the lowest current case than for the highest current case. Thus, the increased theoretical plug thickness with the addition of passive particles suggests that the MCMBs are participating in the particle chains and joining the plug. Wilson et al. found a jump in the yield stress in Couette flow due to a particle jamming-like mechanism [44]. It is possible that a similar mechanism exists for Poiseuille flow.

4.6 Conclusions

The introduction of MCMBs into MR fluids reveals the following:

1. Enhancement in the fluids' yield properties are present in flow mode, but not in shear mode. This is likely due to the migration of particles during rheometer tests.

2. Yield force is a nonlinear increasing function of ϕ_C.

3. For fluids with the same ϕ_{Fe}, increasing ϕ_C produces higher yield forces.

4. Less additional weight is required to increase the yield force by a specified amount when adding MCMBs than when adding CIPs.

5. The MCMBs have greater durability in MR fluid than the glass beads do, with yield force enhancement persisting up to 5 km of piston travel.

6. Using approximate parallel plate analysis reveals an increase in plug thickness with increasing ϕ_C suggesting that the MCMBs are joining the plug as part of the particle chains.

Future work which would enhance the results of this study include more robust characterization of the effect and endurance properties of the MCMBs by testing additional volume fractions of the carbon and iron and testing the fluid with additional cycles.

Chapter 5: Overall Conclusions and Future Work

5.1 Conclusions

The previous two studies comprise an investigation into a control algorithm and working fluid for a magnetorheological energy absorber for enhanced crashworthiness. Chapter 2 outlined an existing control algorithm with its benefits and limitations. Chapter 3 demonstrated the capabilities of the addition of a bumper and use of YFO control to reduce the peak magnitude of jerk. This refinement of the SL control algorithm results in a more comprehensive definition of a 'soft landing' where not only the velocity, but also the acceleration and jerk are brought down to zero. There are however limitations to the YFO control and its applicability is limited to a range of impact velocities. This range could be widened if weights were given to the constraints, if the yield force was allowed to vary throughout the stroke of the MREA, or if a multi-stage control algorithm were implemented. Both SL control and YFO control reveal a need for a wide range of available yield forces. Chapter 4 investigates the enhancement of MR fluid yield force via the incorporation of mesocarbon microbeads. The use of MCMBs does result in a yield force enhancement which is a nonlinearly increasing function of MCMB volume fraction. When subjected to an endurance study, a fluid with 5 vol% MCMBs did not show any signs of reduction in the yield force. A weight study revealed that increasing either the MCMBs or CIPs by the same volume percent resulted in a higher increase in yield force per additional weight for the MCMBs. Finally, it was suggested that the MCMBs were contributing to the plug thickness, potentially acting with a particle jamming-like mechanism.

5.2 Future Work

These two studies produce several courses for future work. A few potential areas for future research are as follows:

1. While studies exist which have investigated the effect of jerk on the human body, this study suggests a more complete investigation of the effect of jerk.
2. The optimization algorithm used to minimize the jerk provides a powerful tool which could be augmented for a multiobjective optimization problem, for varying of the yield force, or other potential changes which could improve occupant protection capabilities.
3. The use of an appropriate surfactant package could enhance the stability of the MCMB-enhanced fluids and potentially produce favorable effects in the rheometer tests.
4. Tests of further MCMB and CIP concentrations could provide a more robust characterization of the effect of the MCMBs.
5. It was also suggested during the SMART ECCOMAS 2019 conference in Paris,

France that frequency testing of the passive particle-enhanced fluids be conducted.

6. An integrative, multidisciplinary approach to designing an MREA vertically stroking crew seat could involve a strategic combination of the two projects. Once a control algorithm has been developed that minimizes an occupant's potential for injury when experiencing crashes with a V_0 range of 4-13 m/s while satisfying physical constraints and injury thresholds, a fluid that meets the necessary passive damping and yield force range could be developed.

Appendix A: Integration of MREA Governing Equation to Obtain Velocity, Displacement, Time to Reach Soft Landing, and Soft Landing Optimal Yield Force

The governing equation, Equation 2.3, is re-written below for clarity.

$$\dot{V} + \frac{c_{MR}}{m} V = -\frac{(mg + f_y sgn(\dot{x}))}{m} \tag{A.1}$$

Using the method of integrating factors, let $\tau(t)$ be the integrating factor and multiply both sides of the equation by τ.

$$\Rightarrow \tau \frac{dV}{dt} + \tau \frac{c_{MR}}{m} V = -\frac{(mg + f_y sgn(V))}{m} \tau \tag{A.2}$$

Notice that

$$\begin{aligned} \frac{d(\tau V)}{dt} &= \tau \frac{dV}{dt} + V \frac{d\tau}{dt} \\ \Rightarrow \frac{d\tau}{dt} &= \tau \left(\frac{c_m}{m} \right) \end{aligned} \tag{A.3}$$

So

$$\begin{aligned} \frac{d\tau/dt}{\tau} &= \frac{c_{MR}}{m} \\ \Rightarrow \int \frac{d\tau}{\tau} &= \int \frac{c_{MR}}{m} dt \\ \Rightarrow \ln(\tau) &= \frac{tc_m}{m} + C_1 \\ \Rightarrow \tau = C_2 e^{tc_{MR}/m} & \text{ where } C_2 = e^{C_1} \end{aligned} \tag{A.4}$$

Substituting in for τ:

$$C_2 e^{tc_{MR}/m}\frac{dV}{dt} + C_2 e^{tc_{MR}/m}\frac{c_{MR}V}{m} = -\frac{(mg + f_y sgn(V))}{m} C_2 e^{tc_{MR}/m}$$

Eliminating C_2 and remembering that $\frac{d(\tau V)}{dt} = \tau\frac{dV}{dt} + V\frac{d\tau}{dt}$:

$$\begin{aligned} \frac{d}{dt}\left(e^{tc_{MR}/m}V\right) &= -\frac{(mg + f_y sgn(V))}{m} e^{tc_{MR}/m} \\ \int d(e^{tc_{MR}/m}V) &= -\int \frac{mg + f_y sgn(V)}{m} e^{c_{MR}/m} dt \\ e^{tc_{MR}/m}V &= -\frac{(mg + f_y sgn(V))}{c_{MR}} e^{c_{MR}/m} + C_3 \\ V &= -\frac{(mg + f_y sgn(V))}{c_{MR}} + C_3 e^{-tc_{MR}/m} \end{aligned} \tag{A.5}$$

Using the initial condition $V(0) = -V_0$:

$$-V_0 = -\frac{(mg + f_y sgn(V))}{c_m} + C_3 \Rightarrow C_3 = \frac{(mg + f_y sgn(V))}{c_m} - V_0 \tag{A.6}$$

leading to:

$$V = -V_0 e^{-tc_{MR}/m} - \frac{(mg + f_y sgn(V))}{c_{MR}}(1 - e^{-tc_{MR}/m}) \tag{A.7}$$

To obtain the displacement solution:

$$\begin{aligned} \frac{dx}{dt} &= -V_0 e^{-tc_{MR}/m} - \frac{(mg + f_y sgn(V))}{c_{MR}}(1 - e^{-tc_{MR}/m}) \\ \int dx &= \int \left[-V_0 e^{-tc_{MR}/m} - \frac{(mg + f_y sgn(V))}{c_{MR}}(1 - e^{-tc_{MR}/m}) \right] dt \\ x &= -V_0\left(-\frac{m}{c_{MR}}\right)e^{-tc_{MR}m} - \frac{(mg + f_y sgn(V))}{c_{MR}}(t + \left(\frac{m}{c_{MR}}\right)e^{-tc_{MR}/m}) + C_4 \end{aligned} \tag{A.8}$$

Using initial condition $x(0) = 0$

$$\begin{aligned} 0 &= V_0\left(\frac{m}{c_{MR}}\right) - \frac{(mg + f_y sgn(V))}{c_{MR}}\left(\frac{m}{c_{MR}}\right) + C_4 \\ \Rightarrow C_4 &= -V_0\left(\frac{m}{c_{MR}}\right) + \frac{(mg + f_y sgn(V))}{c_{MR}}\left(\frac{m}{c_{MR}}\right) \end{aligned}$$

Leading to:

$$x = -\frac{V_0 m}{c_{MR}}(1 - e^{-tc_m/m}) - \frac{(mg + f_y sgn(V))}{c_{MR}}(t - \frac{m}{c_{MR}} + \frac{m}{c_{MR}}e^{-tc_{MR}/m}) \tag{A.9}$$

Implementing the soft landing condition of $V(t_f) = 0$:

$$\begin{aligned}
\left(V_0 - \frac{(mg + f_y sgn(V))}{c_{MR}}\right) e^{-t_f c_{MR}/m} &= -\frac{(mg + f_y sgn(V))}{c_{MR}} \\
e^{-t_f c_{MR}/m} &= \frac{-(mg + f_y sgn(V))}{V_0 c_{MR} - (mg + f_y sgn(V))} \\
e^{t_f c_{MR}/m} &= 1 - \frac{c_{MR} V_0}{mg + f_y sgn(V)} \\
t_f &= \frac{m}{c_{MR}} \ln\left(1 - \frac{c_{MR} V_0}{mg + f_y sgn(V)}\right)
\end{aligned} \tag{A.10}$$

Using the second soft landing condition $x(t_f) = -S$:

$$\begin{aligned}
-S &= -\frac{V_0 m}{c_{MR}}(1 - e^{-t_f c_{MR}/m}) \\
&\quad - \frac{(mg + f_y sgn(V))}{c_{MR}}(t_f - \frac{m}{c_{MR}} + \frac{m}{c_{MR}} e^{-t_f c_{MR}/m}) \\
\frac{f_y sgn(V) t_f}{c_{MR}} &= -\frac{V_0 m}{c_{MR}}(1 - e^{-t_f c_{MR}/m}) \\
&\quad - \frac{(mg + f_y sgn(V))}{c_{MR}}(-\frac{m}{c_{MR}} + \frac{m}{c_{MR}} e^{-t_f c_{MR}/m}) - \frac{mgt_f}{c_{MR}} + S
\end{aligned} \tag{A.11}$$

This results in the following expression for yield force

$$\begin{aligned}
f_y sgn(V) &= -\frac{V_0 m}{t_f}(1 - e^{-t_f c_{MR}/m}) \\
&\quad - \frac{(mg + f_y sgn(V))}{t_f}(-\frac{m}{c_{MR}} + \frac{m}{c_{MR}} e^{-t_f c_{MR}/m}) - mg + \frac{S c_{MR}}{t_f}
\end{aligned} \tag{A.12}$$

which can be solved for iteratively.

Appendix B: Integration of Bumper Equation

Integration of expression for undamped spring-mass-damper bumper system.

Remember:

$$y(t) = Ce^{-\zeta\omega_n t}\cos(\omega_d t - \phi) \tag{B.1}$$

Differentiating:

$$\begin{aligned}\dot{y}(t) &= C(-\zeta\omega_n)e^{-\zeta\omega_n t}\cos(\omega_d t - \phi) + Ce^{-\zeta\omega_n t}(-\sin(\omega_d t - \phi)) \\ &= -Ce^{-\zeta\omega_n t}\Big[\zeta\omega_n\cos(\omega_d t - \phi) + \omega_d\sin(\omega_d t - \phi)\Big]\end{aligned} \tag{B.2}$$

Differentiating again:

$$\begin{aligned}\ddot{y}(t) = C\zeta\omega_n e^{-\zeta\omega_n t}&\Big[\zeta\omega_n\cos(\omega_d t - \phi) + \omega_d\sin(\omega_d t - \phi)\Big] \\ &- Ce^{-\zeta\omega_n t}\Big[-\zeta\omega_n\omega_d\sin(\omega_d t - \phi) + \omega_d^2\cos(\omega_d t - \phi)\Big] \\ = Ce^{-\zeta\omega_n t}&\Big\{\Big[(\zeta\omega_n)^2 - \omega_d^2\Big]\cos(\omega_d t - \phi) + \Big[2\zeta\omega_n\omega_d\Big]\sin(\omega_d t - \phi)\Big\}\end{aligned} \tag{B.3}$$

Bibliography

[1] JW Coltman, CV Ingen, NB Johnson, and RE Zimmerman. Aircraft crash survival design guide. volume 2. aircraft design crash impact conditions and human tolerance. Technical Report USAAVSCOM TR-89-D-22B, Simula Inc., 1989.

[2] Karen E Jackson. Advances in rotorcraft crashworthiness: Trends leading to improved survivability 37th alexander a. nikolsky honorary lecture. *Journal of the American Helicopter Society*, 63(2):1–25, 2018.

[3] JW Coltman, C Van Ingen, and F Selker. Crash-resistant crewseat limit-load optimization through dynamic testing with cadavers. Technical Report USAAVSCOM TR-85-D-11, Siimula Inc., 1986.

[4] A Martin Eiband. Human tolerance to rapidly applied accelerations: a summary of the literature. 1959.

[5] Stanley P Desjardins. The evolution of energy absorption systems for crashworthy helicopter seats. *Journal of the American Helicopter Society*, 51(2):150–163, 2006.

[6] Louise A Powell, Norman M Wereley, and John Ulicny. Magnetorheological fluids employing substitution of nonmagnetic for magnetic particles to increase yield stress. *IEEE Transactions on Magnetics*, 48(11):3764–3767, 2012.

[7] Norman M Wereley. Nondimensional Herschel—Bulkley analysis of magnetorheological and electrorheological dampers. *Journal of Intelligent Material Systems and Structures*, 19(3):257–268, 2008.

[8] Stanley P Desjardins, Richard E Zimmerman, Akif O Bolukbasi, and Norman A Merritt. Aircraft crash survival design guide. volume 4. aircraft seats, restraints, litters, and cockpit/cabin delethalization. Technical Report USAAVSCOM TR 89-D-22D, Simula Inc., 1989.

[9] Martin S Annett and Michael A Polanco. System-integrated finite element analysis of a full-scale helicopter crash test with deployable energy absorbers. 2010.

[10] Gregory J Hiemenz, Wei Hu, and Norman M Wereley. Semi-active magnetorheological helicopter crew seat suspension for vibration isolation. *Journal of Aircraft*, 45(3):945–953, 2008.

[11] Caroline VanIngen-Dunn and Marvin K Richards. Feasibility of reducing incidence of low back pain in helicopter pilots using improved crewseat cushions. Technical Report AL-SR-1991-0009, Simula Inc., 1992.

[12] Military Standard-MIL-STD-1290A. Light fixed & rotary-wing aircraft crash resistance, 1988.

[13] Dennis F Shanahan. Crash experience of the US Army Black Hawk helicopter. In *AGARD Conference Proceedings*, volume 532, pages 40–40. North Atlantic Treaty Organization, 1992.

[14] Peter R Payne. Personnel restraint and support system dynamics. Technical Report AMRL-TR-65-127, Frost Engineering Development Corp Denver Co, 1965.

[15] Peter R Payne. Injury potential of ejection seat cushions. *Journal of Aircraft*, 6(3):273–278, 1969.

[16] Stanley P Desjardins and Harold D Harrison. The design, fabrication, and testing of an integrally armored crashworthy crew seat. Technical Report US-AAMRDL Technical Report 71-54, Dynamic Science Engineering Operations, A Division of Marshall Industries, 1972.

[17] Voight R Hodgson, Herbert R Lissner, and Lawrence M Patrick. The effect of jerk on the human spine. In Edward F Byars, Renato Contini, and Verne L Roberts, editors, *Biomechanics monograph*, pages 115–124. American Society of Mechanical Engineers, 1967.

[18] Roy G Fox. Helicopter crashworthiness - part one. *Flight Safety Foundation: Helicopter Safety*, 15(6):1–6, 1989.

[19] Harinder J Singh, Young-Tai Choi, and Norman M Wereley. Optimal control of vertically stroking crew seats employing magnetorheological energy absorbers. In *ASME 2009 Conference on Smart Materials, Adaptive Structures and Intelligent Systems*, pages 539–550. American Society of Mechanical Engineers, 2009.

[20] Norman M Wereley, Young-Tai Choi, and Harinder J Singh. Adaptive energy absorbers for drop-induced shock mitigation. *Journal of Intelligent Material Systems and Structures*, 22(6):515–519, 2011.

[21] Young-Tai Choi and Norman M Wereley. Vibration control of a landing gear system featuring electrorheological/magnetorheological fluids. *Journal of Aircraft*, 40(3):432–439, 2003.

[22] Louise A Powell, Wei Hu, and Norman M Wereley. Magnetorheological fluid composites synthesized for helicopter landing gear applications. *Journal of Intelligent Material Systems and Structures*, 24(9):1043–1048, 2013.

[23] Fei Gao, Yan-Nan Liu, and Wei-Hsin Liao. Optimal design of a magnetorheological damper used in smart prosthetic knees. *Smart Materials and Structures*, 26(3):035034, 2017.

[24] NM Wereley, A Chaudhuri, J-H Yoo, S John, S Kotha, A Suggs, R Radhakrishnan, BJ Love, and TS Sudarshan. Bidisperse magnetorheological fluids using fe particles at nanometer and micron scale. *Journal of Intelligent Material Systems and Structures*, 17(5):393–401, 2006.

[25] Sung Taek Lim, Min Seong Cho, In Bae Jang, and Hyoung Jin Choi. Magnetorheological characterization of carbonyl iron based suspension stabilized by fumed silica. *Journal of magnetism and magnetic materials*, 282:170–173, 2004.

[26] John C. Ulicny, Keith S. Snavely, Mark A. Golden, and Daniel J. Klingenberg. Enhancing magnetorheology with nonmagnetizable particles. *Applied Physics Letters*, 96(23):231903, 2010.

[27] Rebecca A Snyder, Gopalakrishna M Kamath, and Norman M Wereley. Characterization and analysis of magnetorheological damper behavior under sinusoidal loading. *AIAA journal*, 39(7):1240–1253, 2001.

[28] Alan L Browne, Joseph D Mccleary, Chandra S Namuduri, and Scott R Webb. Impact performance of magnetorheological fluids. *Journal of Intelligent Material Systems and Structures*, 20(6):723–728, 2009.

[29] Gang Wang, Gregory Hiemenz, Wei Hu, and Norman M Wereley. A constant stroking load regulator for shock absorption. In *ASME 2011 Conference on Smart Materials, Adaptive Structures and Intelligent Systems*, pages 43–50. American Society of Mechanical Engineers Digital Collection, 2012.

[30] Dennis F Shanahan. Human tolerance and crash survivability. *Pathological Aspects and Associate Biodynamics in Aircraft Accident Investigation*, (RTO-EN-HFM-113), 2004.

[31] Lane R Miller and Charles M Nobles. Methods for eliminating jerk and noise in semi-active suspensions. *SAE transactions*, pages 943–951, 1990.

[32] Mehdi Ahmadian, Xubin Song, and Steve C Southward. No-jerk skyhook control methods for semiactive suspensions. *Journal of vibration and acoustics*, 126(4):580–584, 2004.

[33] S Rakheja and S Sankar. Effectiveness of on-off damper in isolating dynamical systems. *The Shock and Vibration Bulletin*, pages 147–156, 1986.

[34] Quoc-Hung Nguyen and Seung-Bok Choi. Optimal design of a vehicle magnetorheological damper considering the damping force and dynamic range. *Smart materials and Structures*, 18(1):015013, 2008.

[35] Quoc-Hung Nguyen, Young-Min Han, Seung-Bok Choi, and Norman M Wereley. Geometry optimization of mr valves constrained in a specific volume using the finite element method. *Smart Materials and Structures*, 16(6):2242, 2007.

[36] Harinder J Singh and Norman M Wereley. Optimized biodynamic shock attenuation performance using an adaptive seat suspension. In *ASME 2011 Conference on Smart Materials, Adaptive Structures and Intelligent Systems*, pages 387–395. American Society of Mechanical Engineers Digital Collection, 2012.

[37] S Gad, H Metered, A Bassuiny, and AM Abdel Ghany. Multi-objective genetic algorithm fractional-order pid controller for semi-active magnetorheologically damped seat suspension. *Journal of Vibration and Control*, 23(8):1248–1266, 2017.

[38] John H Crews, Michael G Mattson, and Gregory D Buckner. Multi-objective control optimization for semi-active vehicle suspensions. *Journal of sound and Vibration*, 330(23):5502–5516, 2011.

[39] Leonard Meirovitch. *Fundamentals of Vibrations*. Waveland Press, Inc., 2010.

[40] Panos Y. Papalambros and Douglass J. Wilde. *Principles of Optimal Design: Modeling and Computation*. Cambridge University Press, 3 edition, 2017.

[41] The Mathworks, Inc. Matlab.

[42] Jasbir Singh Arora. Chapter 6 - optimum design: Numerical solution process and excel solver. In Jasbir Singh Arora, editor, *Introduction to Optimum Design (Fourth Edition)*, pages 237 – 278. Academic Press, Boston, fourth edition edition, 2017.

[43] D. J. Klingenberg and J. C. Ulicny. *Enhancing Magnetorheology*, chapter 3, pages 422–428. World Scientific, 2011.

[44] Benjamin T Wilson and Daniel J Klingenberg. A jamming-like mechanism of yield-stress increase caused by addition of nonmagnetizable particles to magnetorheological suspensions. *Journal of Rheology*, 61(4):601–611, 2017.

[45] Grum T Ngatu and Norman M Wereley. Viscometric and sedimentation characterization of bidisperse magnetorheological fluids. *IEEE Transactions on Magnetics*, 43(6):2474–2476, 2007.

[46] Anirban Chaudhuri, Norman M Wereley, R Radhakrishnan, and SB Choi. Rheological parameter estimation for a ferrous nanoparticle-based magnetorheological fluid using genetic algorithms. *Journal of intelligent material systems and structures*, 17(3):261–269, 2006.

[47] GT Ngatu, NM Wereley, JO Karli, and Richard Curtis Bell. Dimorphic magnetorheological fluids: exploiting partial substitution of microspheres by nanowires. *Smart Materials and Structures*, 17(4):045022, 2008.

[48] Gopalakrishna M Kamath, Melanie K Hurt, and Norman M Wereley. Analysis and testing of bingham plastic behavior in semi-active electrorheological fluid dampers. *Smart Materials and Structures*, 5(5):576, 1996.

[49] Norman M Wereley and Li Pang. Nondimensional analysis of semi-active electrorheological and magnetorheological dampers using approximate parallel plate models. *Smart Materials and Structures*, 7:732–743, 1998.